PLANETARY SCIENCE

Disequilibrium biosignatures over Earth history and implications for detecting exoplanet life

Joshua Krissansen-Totton,[1,2]* Stephanie Olson,[3] David C. Catling[1,2]

Chemical disequilibrium in planetary atmospheres has been proposed as a generalized method for detecting life on exoplanets through remote spectroscopy. Among solar system planets with substantial atmospheres, the modern Earth has the largest thermodynamic chemical disequilibrium due to the presence of life. However, how this disequilibrium changed over time and, in particular, the biogenic disequilibria maintained in the anoxic Archean or less oxic Proterozoic eons are unknown. We calculate the atmosphere-ocean disequilibrium in the Precambrian using conservative proxy- and model-based estimates of early atmospheric and oceanic compositions. We omit crustal solids because subsurface composition is not detectable on exoplanets, unlike above-surface volatiles. We find that (i) disequilibrium increased through time in step with the rise of oxygen; (ii) both the Proterozoic and Phanerozoic may have had remotely detectable biogenic disequilibria due to the coexistence of O_2, N_2, and liquid water; and (iii) the Archean had a biogenic disequilibrium caused by the coexistence of N_2, CH_4, CO_2, and liquid water, which, for an exoplanet twin, may be remotely detectable. On the basis of this disequilibrium, we argue that the simultaneous detection of abundant CH_4 and CO_2 in a habitable exoplanet's atmosphere is a potential biosignature. Specifically, we show that methane mixing ratios greater than 10^{-3} are potentially biogenic, whereas those exceeding 10^{-2} are likely biogenic due to the difficulty in maintaining large abiotic methane fluxes to support high methane levels in anoxic atmospheres. Biogenicity would be strengthened by the absence of abundant CO, which should not coexist in a biological scenario.

INTRODUCTION

Life produces waste gases that modify an atmosphere's composition, and it will soon be possible to look for such biosignature gases on exoplanets using telescopic observations. In the near future, a high-contrast imaging system coupled to a spectrograph on the Very Large Telescope may allow the detection of biosignature gases on the nearest exoplanets (1). The James Webb Space Telescope (JWST), scheduled to launch in 2019, will search for biosignature gases on transiting exoplanets such as the TRAPPIST-1 system (2, 3). In the 2020s, three large ground telescopes—the European Extremely Large Telescope, the Thirty Meter Telescope, and the Giant Magellan Telescope—could look for oxygen, water vapor, and carbon dioxide on nearby exoplanets (4–6), whereas the Wide-Field Infrared Survey Telescope may also be capable of detecting biosignature gases on planets orbiting close stars (7). In the more distant future, next-generation space telescopes could survey our stellar neighborhood for biosignatures (8, 9).

Considerable attention has been given to O_2 as a biosignature gas because it is challenging to produce in large quantities without oxygenic photosynthesis (10). Although several pathological scenarios have been proposed whereby a terrestrial planet in the habitable zone might accumulate abiotic oxygen, additional contextual information can rule out these false-positive scenarios (10), whereas some doubt the realism of some of these false-positive concepts (11).

However, even if oxygenic photosynthesis is present, it does not guarantee detectable levels of atmospheric oxygen. There was virtually no oxygen in the Archean eon [4.0 to 2.5 billion years ago (Ga)] (12) despite the possible origin of oxygenic photosynthesis by 3.0 Ga (13).

Oxygen levels in the Proterozoic eon (2.5 to 0.541 Ga) are disputed, but some proxy estimates imply remotely undetectable levels (14). More generally, we do not know whether oxygenic photosynthesis is a likely evolutionary development. Oxygenic photosynthesis is enzymatically complex and only evolved once on Earth (15).

For all these reasons, alternative approaches to biosignatures are needed. Previous studies have explored hydrocarbons and their hazes, organosulfur compounds, and biological pigments as biosignatures for anoxic worlds similar to the early Earth [reviewed by Schwieterman et al. (16)], but these approaches rely on specific metabolisms with high productivities.

A more general biosignature, which has not been considered for the early Earth, is atmospheric chemical disequilibrium, evident in the coexistence of two or more long-term incompatible gases (17–20). The modern O_2-CH_4 redox couple is widely believed to be a compelling disequilibrium biosignature because of the short kinetic lifetime (~10 years) of methane in Earth's atmosphere (21, 22), which requires a substantial source flux of CH_4 in excess of reasonable abiogenic sources.

A number of arguments against the concept of disequilibrium biosignatures have been proposed. Kleidon [(23), p. 250] notes that atmospheric disequilibrium between O_2 and CH_4 exists because of incomplete decomposition of organic matter. The power associated with this leakage of unused free energy is a small fraction (0.3%) of power involved in photosynthesis, and so, it is argued that atmospheric chemical disequilibrium is not a good indicator of biospheric activity. However, chemical disequilibrium need not map to the amount of biological production to be a good biosignature—it merely has to reveal the existence of life. The methane flux required to sustain observed quantities of methane in the modern Earth's oxidizing atmosphere is greater than what abiotic processes could plausibly provide, and thus, biological methane leakage must be invoked to explain the persistent disequilibrium. In addition, it has been argued that the disequilibrium in the Earth's atmosphere is merely a reflection of high oxygen levels and that statements

[1]Department of Earth and Space Sciences/Astrobiology Program, University of Washington, Seattle, WA 98195, USA. [2]Virtual Planetary Laboratory, University of Washington, Seattle, WA 98195, USA. [3]Department of Earth Sciences and NASA Astrobiology Institute, University of California, Riverside, Riverside, CA 92521, USA.
*Corresponding author. Email: joshkt@uw.edu

about disequilibrium therefore reduce to statements about oxygen (24). However, in this paper, we show that there was an important biogenic disequilibrium in the anoxic Archean atmosphere.

Previously, we quantified the thermodynamic disequilibrium in solar system atmospheres by taking observed compositions, reacting them numerically to chemical thermodynamic equilibrium, and calculating the Gibbs free energy difference between observed and equilibrium states (25). Earth's purely gas-phase disequilibrium, as measured by available Gibbs free energy, is 1.5 J/mol of atmosphere and largely attributable to the O_2-CH_4 thermodynamic disequilibrium. The magnitude of this disequilibrium is not large compared to the abiogenic disequilibrium calculated for other solar system bodies, but given the kinetic considerations discussed above, CH_4 and O_2 remain a robust disequilibrium biosignature. In contrast, when the Earth's entire fluid envelope (the atmosphere-ocean reservoir) is considered, the disequilibrium is very large (2326 J/mol) due to the coexistence of O_2, N_2, and liquid water. These three species should react to form nitric acid in thermodynamic equilibrium. Krissansen-Totton et al. (25) discuss how this biogenic disequilibrium is potentially detectable on exoplanets similar to the modern Earth.

Although Earth's chemical disequilibrium is large today, how the disequilibrium changed through Earth history has not been quantified—whether it was large in the Precambrian when there was less atmospheric oxygen, and whether biogenic species would have contributed in an anoxic atmosphere. The N_2-O_2-H_2O and O_2-CH_4 disequilibrium biosignatures may not have been present for much of Earth history because the atmosphere had 20 ± 10% O_2 for only the last one-eighth of its history and virtually no O_2 in the Archean [reviewed by Catling and Kasting (26), chap. 10]. Consequently, we seek to calculate the thermodynamic disequilibrium for the Archean, Proterozoic, and Phanerozoic atmosphere-ocean systems. We explore how Earth's atmosphere-ocean disequilibrium has coevolved with life and find that the results suggest a novel disequilibrium biosignature for Archean-like exoplanets.

RESULTS

Approach for calculating thermodynamic disequilibrium

We calculated chemical thermodynamic disequilibrium in the atmosphere-ocean system according to the methodology shown schematically in Fig. 1 and fully described in Materials and Methods. Our MATLAB code is available on the website of the lead author. Given an assumed composition for the atmosphere and ocean of the early Earth, we react the whole system to thermodynamic equilibrium using Gibbs energy minimization. The equilibrium abundances of reactive constituents differ from the initial abundances, but atoms and charge are conserved. We neglect solids and most nonvolatile aqueous species because our focus is on remotely observable disequilibria (justified further in Discussion and in section S1).

To quantify the chemical thermodynamic disequilibrium in a planet's atmosphere-ocean system, we define the "available Gibbs energy" as the difference in Gibbs free energy between the initial (observed) state and the equilibrium state

$$\Phi \equiv G_{(T,P)}(\mathbf{n}_{\text{initial}}) - G_{(T,P)}(\mathbf{n}_{\text{final}}) \qquad (1)$$

The available Gibbs energy, Φ, has units of joules per mole of atmosphere. The vector $\mathbf{n}_{\text{initial}}$ contains the abundances of all the atmospheric and ocean constituents of the initial state, whereas $\mathbf{n}_{\text{final}}$ contains abundances of the final state. This Gibbs free energy difference is the maximum useful work that can be extracted from the system. That is, Φ is the untapped chemical free energy in a planet's atmosphere and so provides our metric of disequilibrium. Note that when we discuss life exploiting the free energy in a planet's atmosphere, we are referring to surface (or subsurface) life consuming atmospheric gases. Although there are microbes that are adapted to survival in the upper troposphere (27), no known organism subsists independently of the surface.

Table 1 shows estimates of the composition of the atmosphere and ocean in the Precambrian, adopted as initial abundances in our
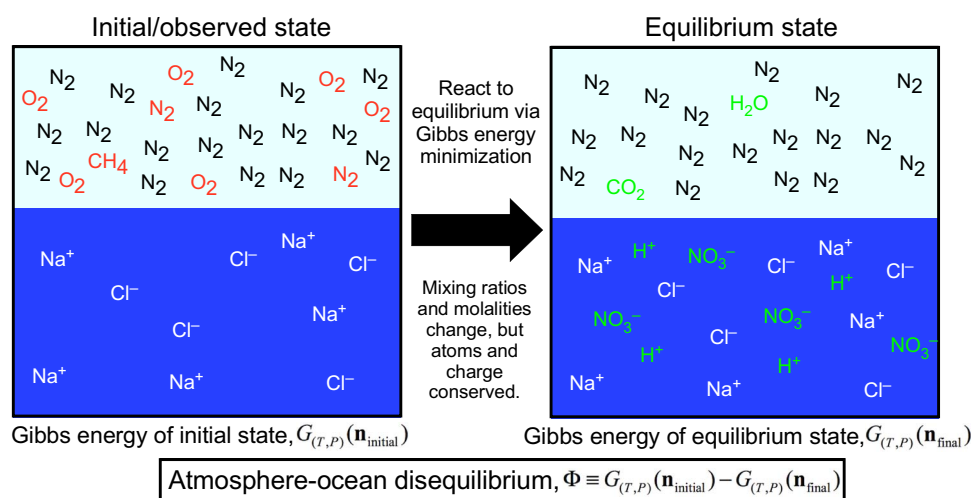
Fig. 1. Schematic of methodology for calculating atmosphere-ocean disequilibrium. We quantify the disequilibrium of the atmosphere-ocean system by calculating the difference in Gibbs energy between the initial and final states. The species in this particular example show the important reactions to produce equilibrium for the Phanerozoic atmosphere-ocean system, namely, the reaction of N_2, O_2, and liquid water to form nitric acid, and methane oxidation to CO_2 and H_2O. Red species denote gases that change when reacted to equilibrium, whereas green species are created by equilibration. Details of aqueous carbonate system speciation are not shown.

Table 1. Assumed initial atmosphere-ocean composition for Archean and Proterozoic.

Atmospheric species	Archean range			Proterozoic range		
	Mixing ratio		Reference/explanation	Mixing ratio		Reference/explanation
	Minimum disequilibrium	Maximum disequilibrium		Minimum disequilibrium	Maximum disequilibrium	
N_2(g)	0.98	0.5	Mixing ratios sum to 1	0.99	0.86	Mixing ratios sum to 1
O_2(g)	1×10^{-10}	2×10^{-7}	(39)	0.0001	0.03	(14, 76)
CH_4(g)	0.0001	0.01	(77)	3×10^{-6}	1×10^{-4}	(78, 79)
CO_2(g)	0.001	0.5	(80, 81)	0.0001	0.1	(80, 81)
H_2(g)	0	0.0001	(59)	0	2×10^{-6}	(82)
N_2O(g)	0	0	No denitrification so negligible production	0	1×10^{-6}	(79, 83)
NH_3(g)	0	1×10^{-9}	(84)	0	0	Negligible in bulk atmosphere
O_3(g)	0	0	Negligible in bulk atmosphere	0	0	Negligible in bulk atmosphere (79)
CO(g)	0	0.001	(59)	0	2×10^{-7}	(82)

Ocean species	Molality (mmol/kg)		Reference/explanation	Molality (mmol/kg)		Reference/explanation
	Minimum disequilibrium	Maximum disequilibrium		Minimum disequilibrium	Maximum disequilibrium	
Na^+	550	586	Charge balance	547	549	Charge balance
Cl^-	546	546	Modern value	546	546	Modern value
SO_4^{2-}	0	0.2	(85, 86)	0.25	5	(87, 88)
H_2S	0	0.004	In euxinic oceans using a Black Sea analog*	0	0.004	In euxinic oceans using a Black Sea analog*
NH_4^+	0	0.050	Set by phosphorus† assuming Redfield ratios and the presence of N fixation, given that N fixation evolved early (89)	0	0.050	Set by phosphorus† assuming Redfield ratios
NO_3^-	0	0	Anoxic bulk ocean	0	0	Anoxic bulk ocean
Alkalinity	4	40	(29); Krissansen-Totton et al., in preparation	1.0	3.0	(29); Krissansen-Totton et al., in preparation
pH	8.0	6.3	Carbon chemistry equilibrium‡	8.4	6.0	Carbon chemistry equilibrium‡

*The concentration of H_2S in the Black Sea is around 400 μmol/kg (90). However, <1 to 10% of the Precambrian seafloor was euxinic (91), which implies <1% euxinia by volume because euxinic continental slopes are much shallower than the deep ocean. Thus, we assumed 4 μmol/kg as an upper limit for bulk ocean aqueous H_2S. †The maximum subsurface concentration of NH_4^+ is ultimately controlled by flux of phosphate from continental weathering. Assuming a modern dissolved phosphate abundance of ~2 μmol/kg, this implies an ammonium abundance of 32 μmol/kg assuming a 1:16 Redfield ratio. Results are largely insensitive to initial abundances of NH_4^+ (Fig. 5). ‡pH is calculated from alkalinity and P_{CO_2} assuming chemical equilibrium.

calculations. Plausible ranges for atmospheric mixing ratios and aqueous species molalities are taken from the literature, which includes proxy estimates and theoretical modeling. For both the Archean and Proterozoic, we calculate two end-member cases, denoted maximum and minimum disequilibrium. The maximum disequilibrium case assumes the largest possible mixing ratios and molalities of reactive species from the literature, whereas the minimum disequilibrium case assumes the converse. In the assumed initial ocean chemistry, [Na^+], a conservative nonreactive ion, is adjusted to achieve charge balance. Similarly, the initial mixing ratio of N_2 is adjusted in every case to ensure that mixing ratios sum to unity.

Calculations were performed at 1-bar surface pressure for which partial pressures are numerically equivalent to mixing ratio constraints, but in the Supplementary Materials, we repeat our Archean calculations at both higher and lower pressures and find that changing atmospheric pressure has little effect on the results. Unless stated otherwise, initial dissolved gas abundances were calculated using Henry's law with coefficients from the National Institute of Standards and Technology (NIST) database (28). The errors introduced by assuming saturation for dissolved species are discussed in section S1 and found to be small. Initial water vapor abundances are also determined using Henry's law. In practice, tropospheric water vapor is spatially and

temporally highly variable (0 to 4%) and controlled by the dynamics of the hydrological cycle, but using Henry's law yields an initial abundance (1.6%) consistent with this empirical range.

Ranges for ocean carbonate alkalinity, which is defined as the charge-weighted sum of carbon-bearing ions, $2[CO_3^{2-}] + [HCO_3^-]$, are based loosely on the study of Halevy and Bachan (29). However, in the Supplementary Materials, we investigate the sensitivity of our results to different assumed alkalinities and find that our key conclusions are unchanged.

Given alkalinity and atmospheric P_{CO_2} (partial pressure of CO_2), we calculate ocean pH, carbonate, and bicarbonate concentrations from equilibrium chemistry. This procedure ensures that out-of-equilibrium carbon chemistry does not contribute to our disequilibrium calculations. Of course, in calculating disequilibria, carbonate speciation may be shifted by the reaction of other species in the system.

A commercial chemical engineering software package called Aspen Plus (version 8.6) was used to validate all the MATLAB calculations reported in this paper [see the study of Krissansen-Totton et al. (25) for full description of its implementation]. Tables comparing MATLAB and Aspen results are reported in section S2. In general, MATLAB and Aspen outputs agree to within 10% or better. Small differences are expected because the thermodynamic models in our MATLAB code differ from those in Aspen Plus. However, unlike the proprietary code, ours is open source and so fully transparent.

Thermodynamic disequilibrium over Earth history

Here, we report results for our maximum and minimum disequilibrium in the Proterozoic and Archean. If the true atmosphere and ocean abundances are bounded by the values in Table 1, then the minimum and maximum disequilibria we calculate will encompass the true disequilibrium of the Earth's atmosphere-ocean system through time.

Figure 2 shows our calculated evolution of Earth's atmosphere-ocean disequilibrium. The modern atmosphere-ocean disequilibrium was analyzed at length by Krissansen-Totton et al. (25). In Fig. 2, the Phanerozoic Earth range was determined by using the abundances from (25) but varying initial oxygen mixing ratios from 0.1 to 0.3, which is the range inferred for the Phanerozoic (30). Two ranges are provided for the Proterozoic representing different assumptions about Proterozoic oxygen. We find that Earth's atmosphere-ocean disequilibrium was the smallest in the Archean, increased with the initial rise of oxygen during the Paleoproterozoic Great Oxidation Event, and then increased again after a second major increase in oxygen during the Neoproterozoic (Fig. 2).

The calculations that follow explain the evolution of Precambrian disequilibrium and which species are out of equilibrium and therefore contributing to the available Gibbs energy. This gives insight into how the disequilibria are affected by life and which species could serve as biosignatures.

## The Proterozoic disequilibrium and species that contribute to it

The available Gibbs energy for the maximum Proterozoic case is 884 J/mol, and the initial and equilibrium abundances for this case are shown in Fig. 3. We computed the contribution of individual reactions to this Gibbs energy by repeating the equilibrium calculation without the reaction products of specific reactions and by checking the results against semianalytic calculations (25).

The largest source of disequilibrium in the Proterozoic is the same as for the modern Earth: The levels of N_2, O_2, and liquid water should not coexist but rather react to form nitric acid

$$5O_2 + 2N_2 + 2H_2O \rightarrow 4H^+ + 4NO_3^- \qquad (2)$$

The depletion of O_2 and the increase in H^+ and NO_3^- are seen in Fig. 3. The formation of nitric acid also drives carbon speciation to a new equilibrium (section S3). Nitric acid formation and subsequent adjustment of carbon speciation contributes ~640 J/mol, the majority of Proterozoic atmosphere-ocean disequilibrium (72%).

Other reactions that contribute to the maximum Proterozoic disequilibrium are shown in section S3. Methane oxidation contributes considerably (75 J/mol) to the maximum Proterozoic disequilibrium because assumed methane abundances are much higher than on the modern Earth

$$CH_4 + 2O_2 \rightarrow 2H_2O + CO_2 \qquad (3)$$
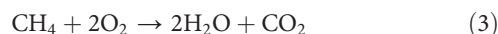
For the minimum Proterozoic case, the disequilibrium is still dominated by nitrate formation, but the available energy is only 9.5 J/mol due to lower initial P_{O_2} (partial pressure of oxygen). Figure S1 shows the initial and equilibrium abundances for the minimum Proterozoic case,
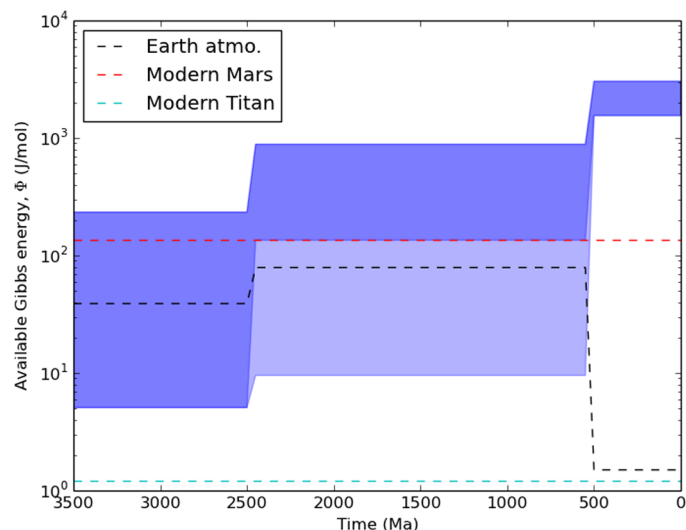

Fig. 2. The evolution of Earth's atmosphere-ocean disequilibrium through time, as measured by available Gibbs free energy. The blue shaded regions show the evolution of Earth's atmosphere-ocean disequilibrium. The wide ranges in the Archean and Proterozoic span our minimum and maximum disequilibrium scenarios. The large ranges are attributable to uncertainties in the atmospheric composition in each eon, mainly uncertain P_{CH_4} in the Archean and uncertain P_{O_2} in the Proterozoic. The two shadings for the Proterozoic represent different assumptions about atmospheric oxygen levels that represent divergent views in the current literature. Darker blue denotes $P_{O_2} > 2\%$ PAL (present atmospheric level), whereas lighter blue denotes $P_{O_2} < 2\%$ PAL. We calculate a secular increase in Earth's atmosphere-ocean disequilibrium over Earth history, correlated with the history of atmospheric oxygen. The black dashed line shows the upper bound of the Earth's atmosphere-only disequilibrium through time. We also include the modern (photochemically produced) disequilibria of Mars (red dashed) and Titan (blue dashed) for comparison (25). The abiotically produced disequilibria of all the other solar system planets are ≪1 J/mol (25).
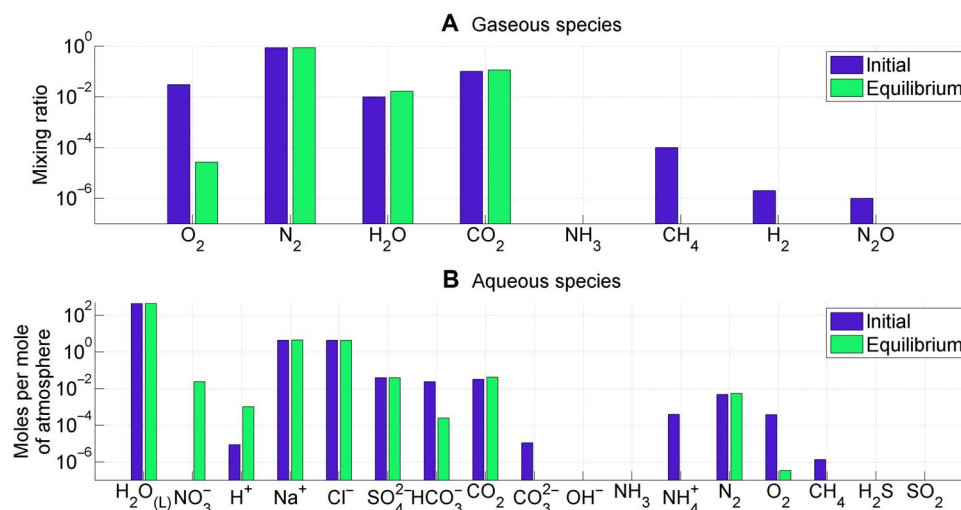
Fig. 3. Atmosphere-ocean disequilibrium in the Proterozoic (maximum disequilibrium scenario). Blue bars denote assumed initial abundances from the literature, and green bars denote equilibrium abundances calculated using Gibbs free energy minimization. Subplots separate (**A**) atmospheric species and (**B**) ocean species. The most important contribution to Proterozoic disequilibrium is the coexistence of atmospheric oxygen, nitrogen, and liquid water. These three species are lessened in abundance by reaction to equilibrium to form aqueous H^+ and NO_3^-. Changes in carbonate speciation caused by the decrease in ocean pH also contribute to the overall Gibbs energy change.

and tables S1 and S2 record numerical abundances for both maximum and minimum Proterozoic cases.

The Archean disequilibrium and species that contribute to it

The initial and equilibrium abundances for the maximum Archean case are shown in Fig. 4. The available Gibbs energy for the maximum Archean case is 234 J/mol, which is dominated by the coexistence of CO_2, N_2, CH_4, and liquid water. These four species should not coexist but rather should react to form ammonium and bicarbonate, depleting almost all atmospheric methane (99.8% of the initial CH_4 is consumed by reaction to equilibrium)

$$5CO_2 + 4N_2 + 3CH_4 + 14H_2O \rightarrow 8NH_4^+ + 8HCO_3^- \quad (4)$$
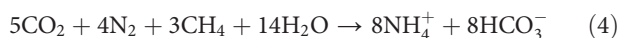
The depletion of CH_4 and increase in NH_4^+ and HCO_3^- are seen in Fig. 4. This reaction alone contributes ~170 J/mol (74%) of the maximum Archean disequilibrium. Other reactions that contribute to the maximum Archean disequilibrium are shown in section S3.

The available energy for the minimum Archean case is 5.1 J/mol, but even in this case, CH_4 is 99.99% depleted with respect to its initial abundance at equilibrium, demonstrating that CH_4 should not coexist in equilibrium with N_2-CO_2-H_2O (liquid) across a broad range of initial conditions. Figure S2 shows the initial and equilibrium abundances for the minimum Archean case. Tables S4 and S5 also record numerical abundances for both maximum and minimum Archean cases.

DISCUSSION
Disequilibria and the history of life

Our results show that Earth's disequilibrium has been strongly affected by life. The evolution of Earth's atmosphere-ocean disequilibrium follows the rise of biogenic oxygen (Fig. 2) similar to how the use of energy by life over Earth history was changed by an anaerobic to aerobic transition (31). Our calculated quantitative evolution of Earth's atmosphere-ocean thermodynamic disequilibrium is also consistent with qualitative speculations about the evolution of free energy dis-

sipation by the biosphere through time [figure 12.5 of Kleidon (23)]. Oxygenic photosynthesis maintains disequilibrium in the Proterozoic and Phanerozoic by replenishing O_2 against O_2 sinks. Oxygenic photosynthesis also replenishes N_2 because the organic matter used in nitrate reduction and subsequent denitrification is produced by oxygenic photosynthesis (although approximately half of the N_2 replenishment comes from outgassing—see below for a more detailed discussion of nitrogen cycling). The emergence of oxygenic photosynthesis and the associated rise in primary productivity increased the disequilibrium of Earth's atmosphere-ocean system. Disequilibrium increased again in the Phanerozoic because oxygenic photosynthesis left a larger imprint on the environment following the Neoproterozoic rise of oxygen.

Before the advent of oxygenic photosynthesis, we calculate that Earth's disequilibrium was probably smaller than at any subsequent time (Fig. 2). If Archean life was exclusively chemotrophic, then it may have decreased a preexisting abiotic disequilibrium, mostly from the H_2-CO_2 pair in the atmosphere (32). With the advent of anoxygenic photosynthesis, the atmosphere-ocean disequilibrium may have increased because additional electron donors become available that were not limited by atmospheric abiotic disequilibrium. For example, Fe-oxidizing phototrophs produce organic carbon through the following net reaction

$$4Fe^{2+} + CO_2 + 11H_2O + h\nu \rightarrow 4Fe(OH)_3 + CH_2O + 8H^+ \quad (5)$$
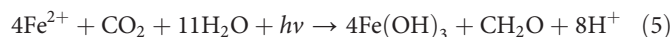
The organic matter produced may then be converted to methane by anaerobic processing, thereby adding to the Archean atmosphere-ocean disequilibrium without the need for outgassed electron donors like H_2; methane is eventually photochemically oxidized to CO_2, thereby closing the cycle. We do not attempt to capture this change in Fig. 2 because we lack sufficient constraints about the advent of types of anoxygenic photosynthesis and their relative influence on atmospheric composition.

However, in both scenarios of anoxygenic photosynthesis and chemotrophy, the Archean biosphere does not drive the atmosphere-ocean system toward equilibrium. Instead, a CH_4-N_2-H_2O-CO_2
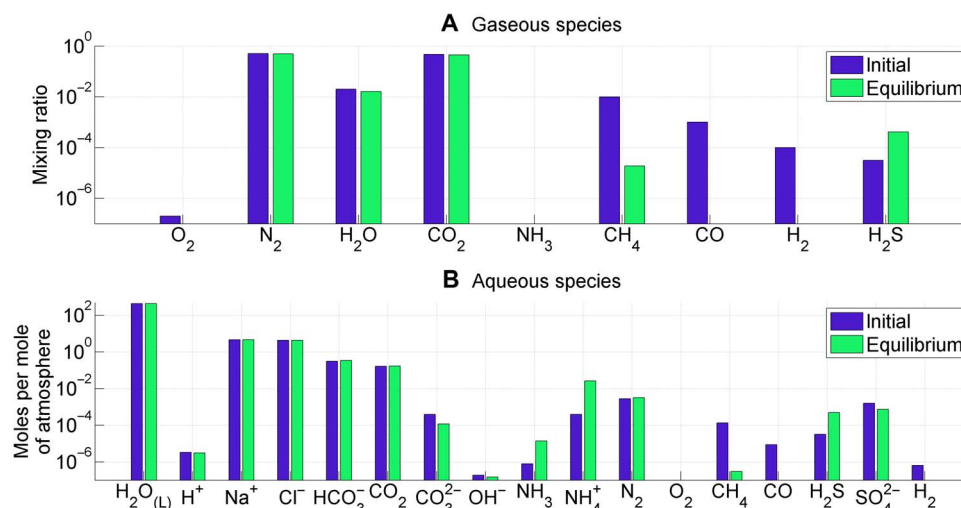
Fig. 4. Atmosphere-ocean disequilibrium in the Archean (maximum disequilibrium scenario). Blue bars denote assumed initial abundances from the literature, and green bars denote equilibrium abundances calculated using Gibbs free energy minimization. Subplots separate (**A**) atmospheric species and (**B**) ocean species. The most important contribution to Archean disequilibrium is the coexistence of atmospheric CH_4, N_2, CO_2, and liquid water. These four species are lessened in abundance by reaction to equilibrium to form aqueous HCO_3^- and NH_4^+. Oxidation of CO and H_2 also contributes to the overall Gibbs energy change.

disequilibrium persists, maintained by methanogens (albeit smaller in the chemotrophic case). After the emergence of oxygenic photosynthesis, but before the rise of oxygen, the CH_4-N_2-H_2O-CO_2 disequilibrium may have increased further due to a larger biological CH_4 flux from the anaerobic processing of organic matter as the productivity of the biosphere increased.

Figure 2 also shows the evolution of Earth's atmosphere-only disequilibrium (bounded by the black dashed line). The atmosphere-only disequilibrium decreases with time and thus does not reflect the rise of oxygen or the growth of primary productivity since 3.5 Ga. This illustrates the importance of including the oceans when quantifying disequilibrium in fluid reservoirs.

An interesting question emerges from this analysis: Given that Earth's atmosphere-ocean system has been massively out of equilibrium since the early Archean, why has life not evolved to consume this "free lunch"? In particular, why have no metabolisms evolved to exploit the N_2-O_2-H_2O disequilibrium present after the Archean? Nitrogen-fixing bacteria and nitrifiers convert N_2 to nitrate, and although the nitrification step yields free energy, no known organism obtains energy by combining these two reactions. Lewis and Randall [(33), pp. 567–568] were the first to recognize that N_2, O_2, and water were out of equilibrium in the Earth system, and they argued that it was fortunate for us that life had not evolved to catalyze their reaction because, otherwise, the atmosphere would have been depleted of oxygen and the oceans turned to dilute nitric acid.

In reality, it is hard to predict what the end result of such evolutionary innovation would be. Atmospheric oxygen would be replenished to some extent by photosynthesis, but nitrogen might be drawn down faster than it could be replenished because there are abundant cations in the crust to neutralize nitric acid oceans, and because dissolved ammonium could be incorporated into clays where it would accumulate. If the atmospheric drawdown were sufficiently severe, then it could even result in a global glaciation due to the loss of pressure broadening from nitrogen. Although anthropic reasoning accounts for why such a metabolism never evolved, a more satisfying explanation is that the kinetic barriers to the N_2-O_2-H_2O reaction are insurmountable. The process by which N_2 is converted to nitrate by Earth life is complex with multiple

steps: Nitrogen fixers expend energy to convert N_2 to NH_3 under anaerobic conditions (or with adaptations to overcome high oxygen levels) to overcome an activation energy barrier (34), and nitrifiers oxidize NH_3 to nitrate under aerobic conditions. Perhaps, the enzymatic machinery required to split the N_2 triple bond and combine these two steps under aerobic conditions is too complex and energy-intensive to maintain.

Practicality of early Earth disequilibrium biosignatures

The most important disequilibrium species in both the Proterozoic (O_2, N_2, ocean) and the Archean (CH_4, N_2, CO_2, ocean) are, in principle, detectable on exoplanets. In the Archean, high CH_4 should be readily detectable (35), and CO_2 has abundant absorption features (36). Nitrogen absorbs at 4.15 µm due to N_4, which could be used to infer N_2 partial pressure (37). Note that it is not necessary to precisely constrain N_2 partial pressure to estimate the CH_4-N_2-CO_2-H_2O thermodynamic disequilibrium. For example, for a maximum Archean disequilibrium scenario with very low N_2 partial pressure (0.02 bar) and high CO_2 (0.95 bar), the available Gibbs energy is 151 J/mol (table S8). So long as there is sufficient N_2 (and CO_2) to react with CH_4 until reaction (4) goes to completion, then a large thermodynamic disequilibrium will exist between N_2, CO, CH_4, and liquid water. Various techniques have been proposed to detect surface oceans including glint, polarization, and surface mapping [reviewed by Fujii et al. (38)] (see section S4 for further discussion).

The remote detectability of oxygen in the Proterozoic atmosphere depends on abundance. If Proterozoic P_{O_2} was <0.1% PAL (present atmospheric level), as has been suggested from one interpretation of Cr isotopes (14), then it may not be possible to detect O_2 on a "Proterozoic Exo-Earth" with next-generation telescopes (35). Extremely low Proterozoic oxygen, however, is difficult to reconcile with photochemical models that show that O_2 levels between 10^{-6} PAL and 0.1% PAL are unstable against small perturbations in the O_2 source flux (39), favoring P_{O_2} closer to the upper boundary used for our maximum disequilibrium calculations. In either case, O_3, a photochemical product of O_2, could be detected even if O_2 itself could not (35, 40).

Regardless of uncertainty about precise abundances of O_2 and CH_4 over Earth history, it is possible to design telescopes capable

of constraining the disequilibrium atmospheric constituents described above. A potential problem for quantifying disequilibrium from observations is its sensitivity to variables that are difficult or impossible to observe, such as ocean composition and ocean volume. In the study of Krissansen-Totton et al. (25), we showed the modern Earth's N_2-O_2-H_2O disequilibrium is relatively insensitive to these variables. The same is true for large Proterozoic disequilibria, which involve the same species.

For the Archean CO_2-N_2-CH_4-H_2O disequilibrium, the equilibrium abundances are insensitive to the unobservable NH_4^+ and HCO_3^- ocean molalities. This insensitivity is shown in Fig. 5, which plots the fractional depletion of methane in equilibrium as a function of initial aqueous species molalities. Unless both NH_4^+ and HCO_3^- are extremely high, methane should be depleted in equilibrium. Section S4 shows that Archean disequilibrium is robust to uncertainties in ocean composition, volume, temperature, and pressure. The magnitude of the Archean thermodynamic disequilibrium typically varies by less than a factor of 2 across a wide range of assumptions about ocean pH, alkalinity, salinity, volume, temperatures, and pressure.

Interpretation of early Earth disequilibrium

Would the detection of CH_4, N_2, CO_2, and an H_2O ocean be a reliable exoplanet biosignature? The thermodynamic disequilibria of modern Mars and Titan are overplotted in Fig. 2, and it can be seen that the abiotic photochemical disequilibrium of Mars is comparable in magnitude to the biological disequilibrium of the early Earth. Clearly, the magnitude of atmospheric disequilibrium does not—on its own—indicate the presence of life. Further interpretation is necessary.

In general, atmospheric disequilibria are the product of the generation of free energy balanced by the dissipation of free energy. A large

thermodynamic disequilibrium could be the consequence of either a high free energy generation rate or a low dissipation rate (22). For this reason, to evaluate the CH_4-N_2-CO_2-H_2O disequilibrium biosignature, it is necessary to consider the photochemical lifetime of CH_4 in such an atmosphere (that is, the rate of free energy dissipation) and possible abiotic sources of CH_4 (rate of free energy generation).

Even in reducing atmospheres, CH_4 has a geologically short lifetime. Diffusion-limited hydrogen escape would deplete an Earth-like planet of atmospheric methane in ~30 thousand years [(26), p. 215]. Consequently, we would not expect a CH_4-N_2-CO_2-H_2O (liquid) disequilibrium to persist without a substantial flux of CH_4 from a planet's surface that is typical of biology. We argue below that large abiotic CH_4 fluxes are unlikely and that, where they do occur, they can probably be distinguished by context.

Mantle-derived methane is an implausible abiotic source and could be distinguished by the coexistence of carbon monoxide. Pressure-temperature conditions in the Earth's shallow mantle (<~100 km) strongly favor CO_2 over CH_4. Any deep mantle CH_4 would be converted to CO_2 by rapid equilibration long before reaching the surface (41). For terrestrial planets with a more reducing mantle than Earth, significant CH_4 outgassing is conceivable. However, a highly reducing mantle would also produce huge CO fluxes (see section S5), and because CO has few abiotic sinks and detectable spectral features (42), mantle-derived methane could readily be identified by coexisting CO. In addition, outgassed CO is unlikely to persist in abundance in the atmospheres of inhabited planets because CO is an excellent source of microbial free energy and carbon (43).

A much discussed scenario for abiotic methane generation is through hydrothermal alteration of crustal mafic rocks (serpentinization), which produces H_2, followed by Fischer-Tropsch type (FTT) synthesis. Following the study of Fiebig et al. (44), we estimate the maximum possible abiotic methane flux, F_{CH_4} (mol/year), that could be generated from this process, as follows

$$F_{CH_4} = \frac{P_{Crust}}{M_{FeO}} fr_{FeO} fr_{H_2} fr_{CH_4} \qquad (6)$$

Here, P_{Crust} is the crustal production rate in kilogram per year, M_{FeO} is the molar mass of FeO in kilogram per mole, fr_{FeO} is the weight % (wt %) of FeO in newly produced crust, fr_{H_2} is the maximum fraction of FeO that is converted to H_2 by serpentinization reactions, and fr_{CH_4} is the maximum fractional conversion of H_2 to CH_4 by FTT reactions. Assuming plausible ranges for these unknown variables and sampling their ranges uniformly, we produce a probability distribution for the maximum possible abiotic methane flux.

Today, magma emplacement from ridges, arcs, and plumes is 5.7×10^{13} kg/year (45), and with a generous assumption that crustal production may have been 10× higher on the early Earth, we take crustal production, P_{Crust}, to range from 5.7×10^{13} to 5.7×10^{14} kg/year. Whether these high crustal production rates are likely for terrestrial exoplanets is an open question, given that some argue that Archean Earth's crustal production may not have been much greater than modern (46). In addition, it might be possible to put some constraints on exoplanet crustal production rates from observable planetary properties (47).

Hydrothermal alteration is ultimately limited by the availability of FeO. The Earth's basaltic oceanic crust is ~10 wt % FeO, which would imply a modern FeO production rate of $0.1 \times 5.7 \times 10^{13}/(0.056 + 0.016) =$ 79 Tmol FeO/year. We will allow fractional FeO content, fr_{FeO}, to vary
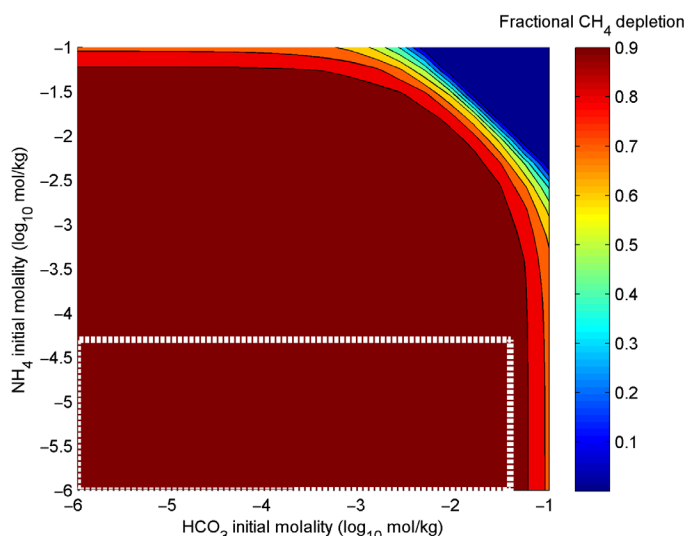

Fig. 5. Sensitivity of Archean disequilibrium to bicarbonate molality and ammonium molality in ocean, quantities that are probably impossible to directly observe for exoplanets. Colors shows fraction of methane depleted in equilibrium, as determined by semianalytic calculations. In this case, $P_{CO_2} = 0.49$ bar, $P_{N_2} = 0.5$ bar, and $P_{CH_4} = 0.01$ bar. As can be seen, most parts of parameter space have high CH_4 depletion, that is, CH_4 is in disequilibrium. Thus, unless both bicarbonate and ammonium molalities are extremely large, detectable quantities of methane are out of equilibrium with an N_2-CO_2 atmosphere and ocean. The white dashed line box denotes the plausible Archean range.

from 10 to 25 wt %, considering possible Mars- or Moon-like crustal compositions.

A key unknown is what fraction of FeO is oxidized by water to liberate H_2, fr_{H_2}. A naïve upper estimate would assume that all the crustal FeO is oxidized to yield H_2 by the following equation

$$3FeO + H_2O \rightarrow Fe_3O_4 + H_2 \tag{7}$$
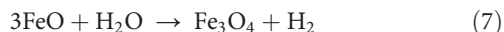
Such an assumption is unrealistic, however. On Earth, multiple lines of evidence suggest that the H_2 production rate from serpentinization is around 0.2 Tmol/year (48, 49), which is 0.25% of the total FeO production, two orders of magnitude less than a one-third theoretical maximum from the stoichiometry of Eq. 7. We take $fr_{FeO} = 0.0025$ as our lower bound for the fractional conversion of H_2 to FeO. On the modern Earth, H_2 production is low because only 12% of crustal Fe^{2+} is converted to Fe^{3+} as water cannot permeate all the oceanic crust (45). Furthermore, only 1 to 2% is due to serpentinization; the remaining 10 to 11% is from oxidation by sulfate, which does not generate H_2 [(26), chap. 10; (45)]. Most of the H_2 produced from serpentinization is derived from ultramafic, slow-spreading crust, which only constitutes 24% of the total crustal production (48). A nonlinear relationship also exists between degree of serpentinization and H_2 production, and for <50% serpentinization, negligible H_2 is generated (49). For the upper bound, we generously assume that the entirety of an Exo-Earth's FeO oxidation is due to H_2-producing serpentinization through Eq. 7, as might occur with more ultramafic crust, giving $fr_{FeO} = 0.12/3 = 0.04$.

The fractional conversion of H_2 to CH_4, fr_{CH_4}, is the final parameter for calculating maximum abiotic CH_4 fluxes. For maximum conversion, we assume that all H_2 makes CH_4 via FTT synthesis

$$CO_2 + 4H_2 \rightarrow 2H_2O + CH_4 \tag{8}$$
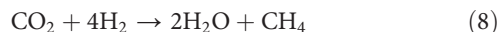
That is, we assume $fr_{CH_4} = 0.25$, aware that this is an overestimate. The conversion of CO_2 to CH_4 by Eq. 8 is thermodynamically favorable in low-temperature hydrothermal systems, but it is unclear whether natural systems can overcome kinetic barriers on a global scale without biological catalysts. Although evidence from field studies suggests that abiotic methane is generated in some hydrothermal systems (44, 50), laboratory experiments typically find very low methane yields from FTT synthesis from olivine. High experimental methane production has been reported (51, 52), but similar experiments with ^{13}C-labeled carbon have shown that the methane produced is derived from background organic carbon contamination (53, 54). Only very specific laboratory conditions yield high CH_4 production from olivine. For example, when pressure is low enough for gas-phase reactions, abiotic CH_4 production is high (53), but it is unlikely that gas-phase reactions would occur at great depth in the crust (44). Similarly, the presence of Fe-Ni catalysts enables CH_4 production (55), but most of Earth's crust is not sufficiently reducing to have such catalysts (41). Guzmán-Marmolejo et al. (56) argued that CH_4 production is further restricted by CO_2 availability in the crust, limiting H_2/CH_4 ratios to ~13. Higher CO_2 concentrations are unlikely to overcome this restriction because Fe^{2+} will be incorporated into siderite rather than form magnetite and H_2 (57). Empirically, H_2/CH_4 ratios in hydrothermal systems are highly variable (48), so it is clear that the kinetic barriers to CH_4 formation and CO_2 limitations are generally present.

For our lower bound on fr_{CH_4}, we will adopt the empirical average from ultramafic-hosted hydrothermal fluids, $H_2/CH_4 = 12$ [table 1 of Keir (48)], which implies $fr_{CH_4} = 1/16$, although this likely overestimates global methane production for the reasons discussed above.

Figure 6 shows the probability distribution for F_{CH_4} obtained by uniformly sampling our chosen ranges for P_{Crust}, fr_{FeO}, fr_{H_2}, and fr_{CH_4}. Both the modern biological methane flux (58) and plausible biological Archean fluxes (59) are much larger than the distribution of maximum abiotic fluxes. On the basis of current understanding, the conditions required to generate large fluxes of abiotic methane are specific and implausible: All unknown variables need to be at the high end of their ranges, and our upper estimate for fr_{H_2} must be an underestimate. However, underestimation of fr_{H_2} is implausible because for fast rates of crustal production, fractional conversion of FeO to H_2 will, if anything, be lower than on Earth because water will permeate a smaller fraction of the total crust given faster spreading rates and thicker crust. In addition, the gas-phase reactions required to overcome kinetic barriers to CH_4 production will be inhibited at greater crustal thicknesses (44).

Impacts have also been proposed as a source of abiotic methane. During an impact, Fe or Ni catalysts in an asteroid could produce CH_4 from CO and H_2. Kress and McKay (60) modeled the kinetics of CH_4 production during the cooling of an impactor fireball and concluded that this could produce an abiotic methane flux during the late heavy bombardment greater than the modern Earth's biological flux. However, an exceptionally high mass flux is required. Using more plausible mass fluxes, Kasting (61) estimated an abiotic methane flux from impactors to be only ~0.3 Tmol/year at 3.8 Ga. This could potentially be increased to 1 Tmol/year if all impact ejecta are serpentinized. However, this too is unrealistically large because complete 12:1 FeO oxidation to CH_4 production is far from guaranteed, as discussed above. In any case, for terrestrial exoplanets, it may be possible to rule out large impactor fluxes from the system age, dust levels, or the absence of transiting planetesimals. For very high impactor fluxes, observable atmospheric consequences such as dust or CO may be detectable.

We conclude that large abiotic sources of CH_4 are either improbable or identifiable with other observations. Furthermore, the rich absorption
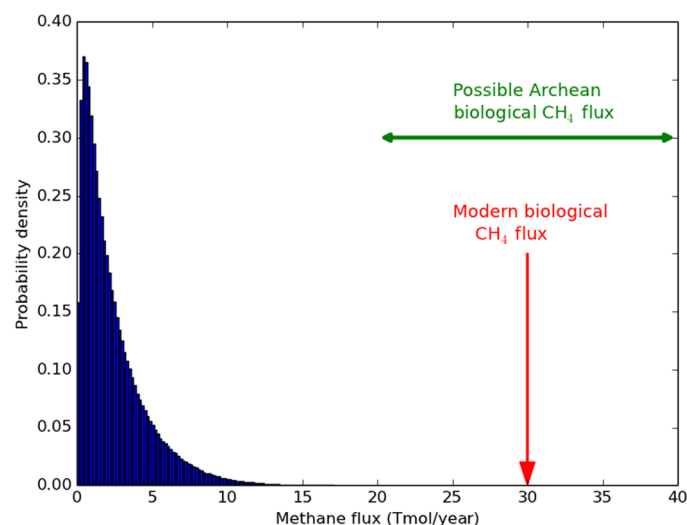

Fig. 6. Probability distribution for maximum abiotic methane production from serpentinization on Earth-like planets. This distribution was generated by sampling generous ranges for crustal production rates, FeO wt %, maximum fractional conversion of FeO to H_2, and maximum fractional conversion of H_2 to CH_4, and then calculating the resultant methane flux 1 million times (see the main text). The modern biological flux (58) and plausible biological Archean flux (59) far exceed the maximum possible abiotic flux. These results support the hypothesis that the co-detection of abundant CH_4 and CO_2 on a habitable exoplanet is a plausible biosignature.

spectra of CO_2, CH_4, and water vapor mean that they are the most readily detectable gases on an exoplanet with an anoxic atmosphere in the near future. Confirmation of a liquid water ocean and atmospheric N_2 that contribute to the full disequilibrium of an Archean Earth twin would require follow-up observations with next-generation space telescopes. However, the detection of CO_2 and CH_4 alone on a habitable exoplanet is a potential disequilibrium biosignature because carbon is present at the extreme ends of the redox ladder (the +4 and −4 states). This CO_2-CH_4 disequilibrium pair is more compelling than CH_4 alone, which could be primordial from a migrated icy world or outgassed from an extremely reducing mantle. An atmosphere rich in CO_2 and CH_4 has been proposed to explain a warm early Mars (62), but this atmosphere would be very transient (<1 million years) because CH_4 released from clathrates would be rapidly photodissociated.

Kinetic and geological considerations
The mere detection of CO_2 and CH_4 (and the absence of CO) does not necessarily imply the presence of life. Instead, it is desirable to calculate the necessary methane source flux given observed atmospheric abundances and the stellar spectrum (56). If the inferred source flux is greater than any known plausible abiotic mechanism (Fig. 6), or if plausible abiotic fluxes can be ruled out by contextual information, then life would be left as a reasonable hypothesis. For planets with anoxic atmospheres such as the CO_2-CH_4-N_2 atmospheres considered here, the methane abundance is set by the balance between photochemical destruction of methane with subsequent diffusion-limited hydrogen escape and the methane source flux from the surface (see section S6 for details). Thus, given an observed atmospheric CH_4 abundance, it is possible to infer the minimum CH_4 flux required to maintain this. Calculations (section S6) suggest that CH_4 abundances in excess of 10^{-3} imply methane source fluxes in excess of 7 Tmol/year, which is likely biological, whereas CH_4 abundances in excess of 10^{-2} imply methane source fluxes in excess of 50 Tmol/year, which is very likely biological (compare Fig. 6), when seen in combination with CO_2 and the absence of CO. These results are largely independent of stellar type, but more precise photochemical calculations ought to be applied in the future to better estimate implied fluxes from abundances.

The CO_2-CH_4 pair might be the most easily detectable exoplanet biosignature. For habitable planets around M-dwarfs with Earth-like biogenic fluxes, the transit transmission features from CO_2 and CH_4 may require shorter integration times to resolve than O_2 or O_3 features with JWST (63).

The kinetics and geological cycling of atmospheric nitrogen are also worth considering, given their contribution to disequilibria in both anoxic and oxic atmospheres. In (25), we presented a calculation to show that if life disappeared from Earth, lightning would convert atmospheric N_2 and O_2 to nitrate, depleting atmospheric oxygen in 20 to 200 Ma. In contrast, it has been argued that nitrate may be reduced to ammonia in mid-ocean ridge hydrothermal systems, which can then return to the atmosphere and be photochemically oxidized back to N_2 (64). However, the reduction of nitrate will yield ammonium, which is readily sequestered into silicates (65, 66). Nitrogen-bearing crust may then be subducted, where some nitrogen may return to the atmosphere via arc volcanism, but the rest will continue to the mantle because of the stability of ammonium-bearing silicates at high temperatures (67). It is therefore reasonable to expect an N_2-O_2-H_2O disequilibrium to disappear without the continuing influence of life, although the precise time scale for the depletion of oxygen and nitrogen will depend on geological cycling that is difficult to quantify. Atmospheric N_2 persists

on Venus because it is in equilibrium with the CO_2-dominated atmosphere (25) and there is no mechanism to draw down N_2 into the crust because of the lack of water.

Solid-state disequilibria
We have not included solid states of matter in our equilibrium calculations. In reality, if the modern Earth's atmosphere-ocean system were allowed to relax to equilibrium, then much of the atmospheric O_2 would react with the crust via oxidative weathering, and some dissolved carbon may form carbonate-bearing rocks. There is also a large disequilibrium between organic carbon and ferric iron in the crust, both of which have accumulated over time from photosynthesis and hydrogen escape, that far exceeds the disequilibrium in the fluid reservoir (25). Although there are 3.7×10^{19} mol O_2 in the atmosphere and oceans, there are 5.1×10^{20} mol O_2 equivalent Fe^{3+} and sulfate in sedimentary rocks, and ~2×10^{21} mol O_2 equivalent excess Fe^{3+} in igneous and metamorphic rocks (68). These crustal rocks are in disequilibrium with the <1.3×10^{21} mol O_2 equivalent reduced carbon in the crust (68). We therefore expect the biogenic disequilibrium in Earth's crustal reservoir to be several orders of magnitude larger than that of the atmosphere-ocean system (25).

However, we chose to ignore solid species because we are interested in remotely detectable disequilibrium biosignatures; detailed crustal compositions cannot be measured for exoplanets, and so, we restrict ourselves to the observable fluid reservoirs. Adding solid phases would not diminish any of the disequilibria described in our analysis but would potentially make the total available energy larger.

One potentially detectable solid-state disequilibrium not considered here is the disequilibrium between atmospheric oxygen and reduced carbon on the surface in the form of biomass [(23), p. 336]. In principle, surface biomass is detectable through the vegetative red edge (16). However, on the modern Earth, even if all the surface biomass (4.4×10^{17} Tmol C) were oxidized, only 1% of atmospheric oxygen would be depleted (69). Biomass oxidation through the following reaction yields 478 kJ/mol

$$CH_2O + O_2 \rightarrow CO_2 + H_2O \tag{9}$$
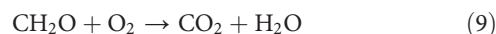
Therefore, the available energy from oxidizing all surface biomass is approximately $(4.4 \times 10^{17}$ mol $\times 478$ kJ/mol$)/(1.8 \times 10^{20}$ mol$) = 1200$ J/mol of atmosphere. This dwarfs the ~1 J/mol from atmospheric methane oxidation but is only half the size of the N_2-O_2-H_2O disequilibrium on the modern Earth.

The simultaneous detection of atmospheric oxygen and a vegetative red edge would obviously be a more compelling biosignature than oxygen alone. However, we do not account for surface biomass in our disequilibrium through time calculations because quantifying surface organic biomass on exoplanets would be extremely challenging. Tinetti et al. (70) showed that the vegetative red edge is potentially detectable with next-generation direct imaging, though challenging with realistic clouds. However, it is not possible to map a red edge detection to surface biomass because near-infrared reflectance depends on numerous vegetation properties such as leaf thickness and canopy structure (71). Tinetti et al. (70) also considered marine plankton detectability and found that even on planets with shallow oceans and an order of magnitude more plankton than the modern Earth, the disc-integrated spectral features would be weaker than the vegetation signal.

CONCLUSIONS

Given current knowledge of the evolution of the atmosphere since the Archean, we calculate that Earth's atmosphere has been in thermodynamic chemical disequilibrium since the early Archean as a result of life. The magnitude of this disequilibrium has increased through time, correlated with increases in atmospheric oxygen and probable growth in biomass. The contributions to disequilibrium from solid states of matter were not included in these calculations because our focus is on properties that would be remotely detectable on exoplanets in the future.

In the Proterozoic and Phanerozoic, the coexistence of N_2, O_2, and liquid H_2O was the largest contributor to chemical disequilibrium. Both N_2 and O_2 are replenished by biology, and this disequilibrium would not persist in the absence of life because almost all the O_2 would be converted to nitric acid in the ocean. A smaller thermodynamic contribution to disequilibrium came from the CH_4-O_2 couple, which remains a compelling biosignature due to the short kinetic lifetime of CH_4 in O_2-rich atmospheres.

In the Archean, we show that likely levels of N_2, CH_4, and CO_2 in the presence of liquid H_2O were the largest contributors to disequilibrium. Without life continuously replenishing atmospheric CH_4, this disequilibrium would not have persisted because CH_4 would have been photolytically destroyed in the upper atmosphere. Large abiogenic fluxes of CH_4 (>10 Tmol/year) needed to support high abiogenic CH_4 abundances are very unlikely to occur on Earth-like exoplanets, and where they do occur, they can probably be identified through context.

The CH_4-N_2-CO_2-H_2O disequilibrium is thus a potentially detectable biosignature for Earth-like exoplanets with anoxic atmospheres and microbial biospheres. The simultaneous detection of abundant CH_4 and CO_2 (and the absence of CO) on an ostensibly habitable exoplanet would be strongly suggestive of biology. Specifically, methane mixing ratios >10^{-3} would imply surface fluxes that are potentially biological, whereas mixing ratios >10^{-2} would imply surface fluxes that are likely biological. Biology allows for the coexisting large redox separation of CH_4 and CO_2 and also readily consumes CO.

MATERIALS AND METHODS
Multiphase disequilibrium calculations

The methodology described here updates that used by Krissansen-Totton et al. (25). To calculate thermodynamic equilibrium for multiphase systems, we followed Karpov et al. (72) and used the following expression for the Gibbs energy of a multiphase system (relative to some reference state)

$$\Delta G_{(T,P)} = \sum_i c_i n_i + \sum_\alpha \sum_{i \in \alpha} n_i RT \ln(n_i/n_\alpha) - \sum_{j = \text{aqueous species}} n_j RT \ln(n_w/n_{aq})$$

$$c_i = \begin{cases} \Delta_f G^\circ_{i(T,P)} + RT \ln(\gamma_{fi}) + RT \ln(P), & i \in \text{gas} \\ \Delta_f G^\circ_{i(T,P)} + RT \ln(\gamma_{aw}), & i \in \text{water} \\ \Delta_f G^\circ_{i(T,P)} + RT \ln(\gamma_{ai}) + RT \ln(55.5084), & i \in \text{aqueous} \end{cases}$$

(10)

Here, we have simplified equations in (72) to exclude solid phases and nonwater pure liquids because we do not consider such systems in

this study. The variables are defined as follows: n_i is the number of moles of the ith species (note that the vector $\mathbf{n}$ consists of the set of n_i); $\Delta_f G^\circ_i(T, P)$ is the standard free energy of formation for the ith species at temperature, T, and pressure, P [see (25) for explanation of how these were calculated and what databases were used]; α is the index for the phase (gaseous, water, or aqueous); n_α is the total number of moles of species in phase α; n_w is the total number of moles of liquid water in the system; n_{aq} is the total number of moles of aqueous species in the system; γ_{aw} is the activity coefficient of water; γ_{ai} is the activity coefficient of the ith aqueous species; γ_{fi} is the fugacity coefficient of the ith gaseous species; R is the universal gas constant; T is the temperature of the system (K), a constant; and P is the pressure of the system (bar), a constant.

To calculate the equilibrium state of the Earth's atmosphere-ocean system, we minimize Eq. 10 subject to the constraint that atoms and charge are conserved, where the latter means that aqueous systems are electroneutral (25).

Several improvements to our multiphase equilibrium calculations have been made from the version described by Krissansen-Totton et al. (25). Most importantly, activity coefficients for all aqueous species are calculated using the Pitzer equations rather than the Truesdell-Jones equation. This proved to be important for accurately capturing the Gibbs energy changes for Archean-like atmosphere-ocean systems. Activity coefficients for cations, M, and anions, X, were specified by the following equations (73)

$$\ln(\gamma_M) = z_M^2 F + \sum_{\text{all anions}} m_a(2B_{Ma} + ZC_{Ma})$$

$$\ln(\gamma_X) = z_X^2 F + \sum_{\text{all cations}} m_c(2B_{cX} + ZC_{cX})$$

where

$$F = -A_\phi \left[\frac{I^{0.5}}{1 + bI^{0.5}} + \frac{2}{b} \ln(1 + bI^{0.5}) \right] + \sum_{\text{all pairs}} m_a m_c B'_{Ma}$$

$$Z = \sum_i m_i |z_i|$$

$$B_{MX} = B_{MX}^{(0)} + B_{MX}^{(1)} f(\alpha_1 I^{1/2}) + B_{MX}^{(2)} f(\alpha_2 I^{1/2})$$

$$f(x) = \frac{2[1 - (1 + x) \exp(-x)]}{x^2}$$

$$B'_{MX} = \frac{B_{MX}^{(1)} f'(\alpha_1 I^{1/2})}{I} + \frac{B_{MX}^{(2)} f'(\alpha_2 I^{1/2})}{I}$$

$$f'(x) = \frac{-2[1 - (1 + x + x^2/2) \exp(-x)]}{x^2}$$

(11)

Here, the variables are defined as follows: m_i is the molality of the ith aqueous species; m_a is the molality of the anion; m_c is the molality of the cation; z_i is the charge of the zth aqueous species; I is the ionic strength of the solution, $I = 0.5 \sum_i m_i z_i^2$; $\alpha_1 = 2.0$ kg$^{0.5}$mol$^{-0.5}$, $\alpha_2 = 0$ kg$^{0.5}$mol$^{-0.5}$ for all binary systems except 2:2 electrolytes; and $\alpha_1 = 1.4$ kg$^{0.5}$mol$^{-0.5}$, $\alpha_2 = 12$ kg$^{0.5}$mol$^{-0.5}$ for 2:2 electrolytes; $b = 1.2$ kg$^{0.5}$mol$^{-0.5}$ and $A_\phi = 0.3915$ kg$^{0.5}$mol$^{-0.5}$ are constants.

$B_{MX}^{(0)}$, $B_{MX}^{(1)}$, $B_{MX}^{(2)}$, C_{MX} are species-specific binary interaction parameters that were obtained from Appelo and Postma (74) and Marion (75). Note that we have adopted a simplified version of the Pitzer equations by ignoring cation-cation and anion-anion interactions, neutral solute parameters, and triple particle parameters. The excellent agreement between MATLAB and Aspen calculations confirms that neglecting

these terms is a reasonable approximation. Methods for calculating fugacity coefficients and the activity of water are the same as those by Krissansen-Totton *et al.* (*25*).

SUPPLEMENTARY MATERIALS

REFERENCES AND NOTES

1. C. Lovis, I. Snellen, D. Mouillet, F. Pepe, F. Wildi, N. Astudillo-Defru, J.-L. Beuzit, X. Bonfils, A. Cheetham, U. Conod, X. Delfosse, D. Ehrenreich, P. Figueira, T. Forveille, J. H. C. Martins, S. P. Quanz, N. C. Santos, H.-M. Schmid, D. Ségransan, S. Udry, Atmospheric characterization of Proxima b by coupling the SPHERE high-contrast imager to the ESPRESSO spectrograph. *Astron. Astrophys.* **599**, A16 (2017).

2. J. K. Barstow, P. G. Irwin, Habitable worlds with JWST: Transit spectroscopy of the TRAPPIST-1 system? *Mon. Not. R. Astron. Soc. Lett.* **461**, L92–L96 (2016).

3. M. Gillon, A. H. M. J. Triaud, B.-O. Demory, E. Jehin, E. Agol, K. M. Deck, S. M. Lederer, J. de Wit, A. Burdanov, J. G. Ingalls, E. Bolmont, J. Leconte, S. N. Raymond, F. Selsis, M. Turbet, K. Barkaoui, A. Burgasser, M. R. Burleigh, S. J. Carey, A. Chaushev, C. M. Copperwheat, L. Delrez, C. S. Fernandes, D. L. Holdsworth, E. J. Kotze, V. Van Grootel, Y. Almleaky, Z. Benkhaldoun, P. Magain, D. Queloz, Seven temperate terrestrial planets around the nearby ultracool dwarf star TRAPPIST-1. *Nature* **542**, 456–460 (2017).

4. I. Snellen, R. de Kok, J. L. Birkby, B. Brandl, M. Brogi, C. Keller, M. Kenworthy, H. Schwarz, R. Stuik, Combining high-dispersion spectroscopy with high contrast imaging: Probing rocky planets around our nearest neighbors. *Astron. Astrophys.* **576**, A59 (2015).

5. I. A. G. Snellen, R. J. de Kok, R. le Poole, M. Brogi, J. Birkby, Finding extraterrestrial life using ground-based high-dispersion spectroscopy. *Astrophys. J.* **764**, 182 (2013).

6. F. Rodler, M. López-Morales, Feasibility studies for the detection of O_2 in an earth-like exoplanet. *Astrophys. J.* **781**, 54 (2014).

7. D. Spergel, N. Gehrels, C. Baltay, D. Bennett, J. Breckinridge, M. Donahue, A. Dressler, B. S. Gaudi, T. Greene, O. Guyon, C. Hirata, J. Kalirai, N. J. Kasdin, B. Macintosh, W. Moos, S. Perlmutter, M. Postman, B. Rauscher, J. Rhodes, Y. Wang, D. Weinberg, D. Benford, M. Hudson, W. -S. Jeong, Y. Mellier, W. Traub, T. Yamada, P. Capak, J. Colbert, D. Masters, M. Penny, D. Savransky, D. Stern, N. Zimmerman, R. Barry, L. Bartusek, K. Carpenter, E. Cheng, D. Content, F. Dekens, R. Demers, K. Grady, C. Jackson, G. Kuan, J. Kruk, M. Melton, B. Nemati, B. Parvin, I. Poberezhskiy, C. Peddie, J. Ruffa, J. K. Wallace, A. Whipple, E. Wollack, F. Zhao, Wide-Field InfraRed survey telescope-astrophysics focused telescope assets WFIRST-AFTA 2015 report. http://arxiv.org/abs/1503.03757 (2015).

8. J. Dalcanton, S. Seager, S. Aigrain, S. Battel, N. Brandt, C. Conroy, L. Feinberg, S. Gezari, O. Guyon, W. Harris, C. Hirata, J. Mather, M. Postman, D. Redding, D. Schiminovich, H. P. Stahl, J. Tumlinson, From cosmic birth to living earths: The future of UVOIR space astronomy. http://arxiv.org/abs/1507.04779 (2015).

9. B. Mennesson, S. Gaudi, S. Seager, K. Cahoy, S. Domagal-Goldman, L. Feinberg, O. Guyon, J. Kasdin, C. Marois, D. Mawet, M. Tamura, D. Mouillet, T. Prusti, A. Quirrenbach, T. Robinson, L. Rogers, P. Scowen, R. Somerville, K. Stapelfeldt, D. Stern, M. Still, M. Turnbull, J. Booth, A. Kiessling, G. Kuan, K. Warfield, The habitable exoplanet

10. (HabEx) imaging mission: Preliminary science drivers and technical requirements, *SPIE Astronomical Telescopes + Instrumentation*, Edinburgh, UK, 2016 (International Society for Optics and Photonics, 2016).

10. V. S. Meadows, Reflections on O_2 as a biosignature in exoplanetary atmospheres. *Astrobiology* **17**, 1022–1052 (2017).

11. K. J. Zahnle, D. C. Catling, The cosmic shoreline: The evidence that escape determines which planets have atmospheres, and what this may mean for Proxima Centauri b. *Astrophys. J.* **843**, 122 (2017).

12. J. Farquhar, H. Bao, M. Thiemens Atmospheric influence of Earth's earliest sulfur cycle. *Science* **289**, 756–758 (2000).

13. N. J. Planavsky, D. Asael, A. Hofmann, C. T. Reinhard, S. V. Lalonde, A. Knudsen, X. Wang, F. O. Ossa, E. Pecoits, A. J. B. Smith, N. J. Beukes, A. Bekker, T. M. Johnson, K. O. Konhauser, T. W. Lyons, O. J. Rouxel, Evidence for oxygenic photosynthesis half a billion years before the Great Oxidation Event. *Nat. Geosci.* **7**, 283–286 (2014).

14. N. J. Planavsky, C. T. Reinhard, X. Wang, D. Thomson, P. McGoldrick, R. H. Rainbird, T. Johnson, W. W. Fischer, T. W. Lyons, Low Mid-Proterozoic atmospheric oxygen levels and the delayed rise of animals. *Science* **346**, 635–638 (2014).

15. A. H. Knoll, Cyanobacteria and earth history. *Cyanobacteria Mol. Biol. Genom. Evol.* **484** (2008).

16. E. W. Schwieterman, N. Y. Kiang, M. N. Parenteau, C. E. Harman, S. DasSarma, T. M. Fisher, G. N. Arney, H. E. Hartnett, C. T. Reinhard, S. L. Olson, V. S. Meadows, C. S. Cockell, S. I. Walker, J. L. Grenfell, S. Hegde, S. Rugheimer, R. Hu, T. W. Lyons, Exoplanet biosignatures: A review of remotely detectable signs of life. http://arxiv.org/abs/1705.05791 (2017).

17. J. E. Lovelock, A physical basis for life detection experiments. *Nature* **207**, 568–570 (1965).

18. D. R. Hitchcock, J. E. Lovelock, Life detection by atmospheric analysis. *Icarus* **7**, 149–159 (1967).

19. C. S. Cockell, A. Léger, M. Fridlund, T. M. Herbst, L. Kaltenegger, O. Absil, C. Beichman, W. Benz, M. Blanc, A. Brack, A. Chelli, L. Colangeli, H. Cottin, F. Coudé du Foresto, W. C. Danchi, D. Defrère, J.-W. den Herder, C. Eiroa, J. Greaves, T. Henning, K. J. Johnston, H. Jones, L. Labadie, H. Lammer, R. Launhardt, P. Lawson, O. P. Lay, J.-M. LeDuigou, R. Liseau, F. Malbet, S. R. Martin, D. Mawet, D. Mourard, C. Moutou, L. M. Mugnier, M. Ollivier, F. Paresce, A. Quirrenbach, Y. D. Rabbia, J. A. Raven, H. J. A. Rottgering, D. Rouan, N. C. Santos, F. Selsis, E. Serabyn, H. Shibai, M. Tamura, E. Thiébaut, F. Westall, G. J. White, *Darwin*—A mission to detect and search for life on extrasolar planets. *Astrobiology* **9**, 1–22 (2009).

20. C. Sagan, W. R. Thompson, R. Carlson, C. Gurnett, C. Hord, A search for life on Earth from the Galileo spacecraft. *Nature* **365**, 715–721 (1993).

21. R. G. Prinn, J. Huang, R. F. Weiss, D. M. Cunnold, P. J. Fraser, P. G. Simmonds, A. McCulloch, C. Harth, P. Salameh, S. O'Doherty, R. H. J. Wang, L. Porter, B. R. Miller, Evidence for substantial variations of atmospheric hydroxyl radicals in the past two decades. *Science* **292**, 1882–1888 (2001).

22. E. Simoncini, N. Virgo, A. Kleidon, Quantifying drivers of chemical disequilibrium: Theory and application to methane in the Earth's atmosphere. *Earth Syst. Dyn.* **4**, 317–331 (2013).

23. A. Kleidon, *Thermodynamic Foundations of the Earth System* (Cambridge Univ. Press, 2016).

24. S. Seager, W. Bains, The search for signs of life on exoplanets at the interface of chemistry and planetary science. *Sci. Adv.* **1**, e1500047 (2015).

25. J. Krissansen-Totton, D. S. Bergsman, D. C. Catling, On detecting biospheres from chemical thermodynamic disequilibrium in planetary atmospheres. *Astrobiology* **16**, 39–67 (2016).

26. D. C. Catling, J. Kasting, *Atmospheric Evolution on Inhabited and Lifeless Worlds* (Cambridge Univ. Press, 2017).

27. N. DeLeon-Rodriguez, T. L. Lathem, L. M. Rodriguez-R, J. M. Barazesh, B. E. Anderson, A. J. Beyersdorf, L. D. Ziemba, M. Bergin, A. Nenes, K. T. Konstantinidisa, Microbiome of the upper troposphere: Species composition and prevalence, effects of tropical storms, and atmospheric implications. *Proc. Natl. Acad. Sci. U.S.A.* **110**, 2575–2580 (2013).

28. R. Sander, Henry's law constants, in *NIST Chemistry WebBook, NIST Standard Reference Database* (National Institute of Standards and Technology, 1999).

29. I. Halevy, A. Bachan, The geologic history of seawater pH. *Science* **355**, 1069–1071 (2017).

30. R. A. Berner, D. J. Beerling, R. Dudley, J. M. Robinson, R. A. Wildman Jr., Phanerozoic atmospheric oxygen. *Annu. Rev. Earth Planet. Sci.* **31**, 105–134 (2003).

31. O. P. Judson, The energy expansions of evolution. *Nat. Ecol. Evol.* **1**, 0138 (2017).

32. C. B. Pilcher, Biosignatures of early Earths. *Astrobiology* **3**, 471–486 (2003).

33. G. N. Lewis, M. Randall, *Thermodynamics and the Free Energy of Chemical Substances* (McGraw-Hill, 1923).

34. P. Fay, Oxygen relations of nitrogen fixation in cyanobacteria. *Microbiol. Rev.* **56**, 340–373 (1992).

35. C. T. Reinhard, S. L. Olson, E. W. Schwieterman, T. W. Lyons, False negatives for remote life detection on ocean-bearing planets: Lessons from the early Earth. *Astrobiology* **17**, 287–297 (2017).

36. D. C. Catling, J. Krissansen-Totton, N. Y. Kiang, D. Crisp, T. D. Robinson, S. DasSarma, A. Rushby, A. Del Genio, W. Bains, S. Domagal-Goldman, Exoplanet biosignatures: A framework for their assessment. http://arxiv.org/abs/1705.06381 (2017).

37. E. W. Schwieterman, T. D. Robinson, V. S. Meadows, A. Misra, S. Domagal-Goldman, Detecting and constraining N_2 abundances in planetary atmospheres using collisional pairs. *Astrophys. J.* **810**, 57 (2015).

38. Y. Fujii, D. Angerhausen, R. Deitrick, S. Domagal-Goldman, J. L. Grenfell, Y. Hori, S. R. Kane, E. Palle, H. Rauer, N. Siegler, K. Stapelfeldt, K. B. Stevenson, Exoplanet biosignatures: Observational prospects. http://arxiv.org/abs/1705.07098 (2017).

39. K. Zahnle, M. Claire, D. Catling, The loss of mass-independent fractionation in sulfur due to a Palaeoproterozoic collapse of atmospheric methane. *Geobiology* **4**, 271–283 (2006).

40. S. R. Heap, Detecting biomarkers in exoplanetary atmospheres with terrestrial planet finder. *EAS Publ. Ser.* **41**, 517–520 (2010).

41. T. M. McCollom, Laboratory simulations of abiotic hydrocarbon formation in Earth's deep subsurface. *Rev. Mineral. Geochem.* **75**, 467–494 (2013).

42. E. W. Schwieterman, V. S. Meadows, S. D. Domagal-Goldman, D. Deming, G. N. Arney, R. Luger, C. E. Harman, A. Misra, R. Barnes, Identifying planetary biosignature impostors: Spectral features of CO and O_4 resulting from abiotic O_2/O_3 production. *Astrophys. J. Lett.* **819**, L13 (2016).

43. K. Zahnle, R. S. Freedman, D. C. Catling, Is there methane on Mars? *Icarus* **212**, 493–503 (2011).

44. J. Fiebig, A. B. Woodland, J. Spangenberg, W. Oschmann, Natural evidence for rapid abiogenic hydrothermal generation of CH_4. *Geochim. Cosmochim. Acta* **71**, 3028–3039 (2007).

45. C. Lécuyer, Y. Ricard, Long-term fluxes and budget of ferric iron: Implication for the redox states of the Earth's mantle and atmosphere. *Earth Planet. Sci. Lett.* **165**, 197–211 (1999).

46. J. Korenaga, Plate tectonics, flood basalts and the evolution of Earth's oceans. *Terra Nova* **20**, 419–439 (2008).

47. D. Valencia, R. J. O'Connell, D. D. Sasselov Inevitability of plate tectonics on super-Earths. *Astrophys. J., Lett.* **670**, L45 (2007).

48. R. S. Keir A note on the fluxes of abiogenic methane and hydrogen from mid-ocean ridges. *Geophys. Res. Lett.* **37** (2010).

49. M. Cannat, F. Fontaine, J. Escartin, Serpentinization and associated hydrogen and methane fluxes at slow spreading ridges. *Geophys. Monogr. Ser.* 241–264 (2010).

50. A. S. Bradley, R. E. Summons, Multiple origins of methane at the Lost City Hydrothermal Field. *Earth Planet. Sci. Lett.* **297**, 34–41 (2010).

51. C. Oze, L. C. Jones, J. I. Goldsmith, R. J. Rosenbauer, Differentiating biotic from abiotic methane genesis in hydrothermally active planetary surfaces. *Proc. Natl. Acad. Sci. U.S.A.* **109**, 9750–9754 (2012).

52. A. Neubeck, N. T. Duc, D. Bastviken, P. Crill, N. G. Holm, Formation of H_2 and CH_4 by weathering of olivine at temperatures between 30 and 70°C. *Geochem. Trans.* **12**, 6 (2011).

53. T. M. McCollom, Abiotic methane formation during experimental serpentinization of olivine. *Proc. Natl. Acad. Sci. U.S.A.* **113**, 13965–13970 (2016).

54. N. G. Grozeva, F. Klein, J. S. Seewald, S. P. Sylva, Experimental study of carbonate formation in oceanic peridotite. *Geochim. Cosmochim. Acta* **199**, 264–286 (2017).

55. J. Horita, M. E. Berndt, Abiogenic methane formation and isotopic fractionation under hydrothermal conditions. *Science* **285**, 1055–1057 (1999).

56. A. Guzmán-Marmolejo, A. Segura, E. Escobar-Briones, Abiotic production of methane in terrestrial planets. *Astrobiology* **13**, 550–559 (2013).

57. L. C. Jones, R. Rosenbauer, J. I. Goldsmith, C. Oze, Carbonate control of H_2 and CH_4 production in serpentinization systems at elevated P-Ts. *Geophys. Res. Lett.* **37**, L14306 (2010).

58. K. L. Denman, G. Brasseur, A. Chidthaisong, P. Ciais, P. M. Cox, R. E. Dickinson, Couplings between changes in the climate system and biogeochemistry in *Climate Change 2007: The Physical Science Basis*, S. Solomon, Ed. (Cambridge Univ. Press, 2007).

59. P. Kharecha, J. Kasting, J. Siefert, A coupled atmosphere–ecosystem model of the early Archean Earth. *Geobiology* **3**, 53–76 (2005).

60. M. E. Kress, C. P. McKay, Formation of methane in comet impacts: Implications for Earth, Mars, and Titan. *Icarus* **168**, 475–483 (2004).

61. J. F. Kasting, Methane and climate during the Precambrian era. *Precambrian Res.* **137**, 119–129 (2005).

62. E. S. Kite, M. A. Mischna, P. Gao, Y. L. Yung, Climate optimum on Mars initiated by atmospheric collapse. http://arxiv.org/abs/1709.08302 (2017).

63. V. S. Meadows, G. N. Arney, E. W. Schwieterman, J. Lustig-Yaeger, A. P. Lincowski, T. Robinson, S. D. Domagal-Goldman, R. K. Barnes, D. P. Fleming, R. Deitrick, R. Luger, P. E. Driscoll, T. R. Quinn, D. Crisp, The habitability of Proxima Centauri b:

64. J. F. Kasting, D. P. Whitmire, R. T. Reynolds, Habitable zones around main sequence stars. *Icarus* **101**, 108–128 (1993).

65. N. H. Sleep, D. K. Bird, M. T. Rosing, Biological effects on the source of geoneutrinos. *Int. J. Mod. Phys. A* **28**, 1330047 (2013).

66. V. Šucha, P. Uhlík, J. Madejová, S. Petit, I. Kraus, Particle properties of hydrothermal ammonium-bearing illite-smectite. *Clays Clay Miner.* **55**, 36–44 (2007).

67. A. Watenphul, B. Wunder, R. Wirth, W. Heinrich Ammonium-bearing clinopyroxene: A potential nitrogen reservoir in the Earth's mantle. *Chem. Geol.* **270**, 240–248 (2010).

68. D. C. Catling, K. J. Zahnle, C. P. McKay, Biogenic methane, hydrogen escape, and the irreversible oxidation of early Earth. *Science* **293**, 839–843 (2001).

69. D. C. Catling, M. W. Claire, How Earth's atmosphere evolved to an oxic state: A status report. *Earth Planet. Sci. Lett.* **237**, 1–20 (2005).

70. G. Tinetti, V. S. Meadows, D. Crisp, N. Y. Kiang, B. H. Kahn, E. Bosc, E. Fishbein, T. Velusamy, M. Turnbull, Detectability of planetary characteristics in disk-averaged spectra II: Synthetic spectra and light-curves of earth. *Astrobiology* **6**, 881–900 (2006).

71. N. Y. Kiang, J. Siefert, R. E. Blankenship, Spectral signatures of photosynthesis. I. Review of Earth organisms. *Astrobiology* **7**, 222–251 (2007).

72. I. K. Karpov, K. V. Chudnenko, D. A. Kulik, Modeling chemical mass transfer in geochemical processes; thermodynamic relations, conditions of equilibria and numerical algorithms. *Am. J. Sci.* **297**, 767–806 (1997).

73. G. M. Marion, J. S. Kargel, *Cold Aqueous Planetary Geochemistry with FREZCHEM: From Modeling to the Search for Life at the Limits* (Springer Science & Business Media, 2007).

74. C. A. J. Appelo, D. Postma, *Geochemistry, Groundwater and Pollution* (CRC Press, 2005).

75. G. M. Marion, A molal-based model for strong acid chemistry at low temperatures (<200 to 298 K). *Geochim. Cosmochim. Acta* **66**, 2499–2516 (2002).

76. T. W. Lyons, C. T. Reinhard, N. J. Planavsky, The rise of oxygen in Earth's early ocean and atmosphere. *Nature* **506**, 307–315 (2014).

77. J. F. Kasting, L. L. Brown, The early atmosphere as a source of biogenic compounds, in *The Molecular Origins of Life*, A. Brack, Ed. (Cambridge Univ. Press, 1998), pp. 35–56.

78. S. L. Olson, C. T. Reinhard, T. W. Lyons, Limited role for methane in the mid-Proterozoic greenhouse. *Proc. Natl. Acad. Sci. U.S.A.* **113**, 11447–11452 (2016).

79. J. L. Grenfell, S. Gebauer, P. von Paris, M. Godolt, P. Hedelt, A. Patzer, H. Rauer, B. Stracke, Sensitivity of biomarkers to changes in chemical emissions in the Earth's Proterozoic atmosphere. *Icarus* **211**, 81–88 (2011).

80. N. D. Sheldon, Precambrian paleosols and atmospheric CO_2 levels. *Precambrian Res.* **147**, 148–155 (2006).

81. Y. Kanzaki, T. Murakami, Estimates of atmospheric CO_2 in the Neoarchean–Paleoproterozoic from paleosols. *Geochim. Cosmochim. Acta* **159**, 190–219 (2015).

82. A. Segura, K. Krelove, J. F. Kasting, D. Sommerlatt, V. Meadows, D. Crisp, M. Cohen, E. Mlawer, Ozone concentrations and ultraviolet fluxes on Earth-like planets around other stars. *Astrobiology* **3**, 689–708 (2003).

83. A. L. Roberson, J. Roadt, I. Halevy, J. Kasting, Greenhouse warming by nitrous oxide and methane in the Proterozoic Eon. *Geobiology* **9**, 313–320 (2011).

84. E. Wolf, O. Toon, Fractal organic hazes provided an ultraviolet shield for early Earth. *Science* **328**, 1266–1268 (2010).

85. S. A. Crowe, S. Paris, S. Katsev, C. Jones, S.-T. Kim, A. L. Zerkle, S. Nomosatryo, D. A. Fowle, J. F. Adkins, A. L. Sessions, J. Farquhar, D. E. Canfield, Sulfate was a trace constituent of Archean seawater. *Science* **346**, 735–739 (2014).

86. K. S. Habicht, M. Gade, B. Thamdrup, P. Berg, D. E. Canfield, Calibration of sulfate levels in the Archean ocean. *Science* **298**, 2372–2374 (2002).

87. L. C. Kah, T. W. Lyons, T. D. Frank, Low marine sulphate and protracted oxygenation of the Proterozoic biosphere. *Nature* **431**, 834–838 (2004).

88. C. Scott, B. A. Wing, A. Bekker, N. J. Planavsky, P. Medvedev, S. M. Bates, M. Yun, T. W. Lyons, Pyrite multiple-sulfur isotope evidence for rapid expansion and contraction of the early Paleoproterozoic seawater sulfate reservoir. *Earth Planet. Sci. Lett.* **389**, 95–104 (2014).

89. E. E. Stüeken, R. Buick, B. M. Guy, M. C. Koehler, Isotopic evidence for biological nitrogen fixation by molybdenum-nitrogenase from 3.2 Gyr. *Nature* **520**, 666–669 (2015).

90. R. Sweeney, I. Kaplan, Stable isotope composition of dissolved sulfate and hydrogen sulfide in the Black Sea. *Mar. Chem.* **9**, 145–152 (1980).

91. C. T. Reinhard, N. J. Planavsky, L. J. Robbins, C. A. Partin, B. C. Gille, S. V. Lalonde, A. Bekker, K. O. Konhauser, T. W. Lyons, Proterozoic ocean redox and biogeochemical stasis. *Proc. Natl. Acad. Sci. U.S.A.* **110**, 5357–5362 (2013).

92. V. A. Samarkin, M. T. Madigan, M. W. Bowles, K. L. Casciotti, J. C. Priscu, C. P. McKay, S. B. Joye, Abiotic nitrous oxide emission from the hypersaline Don Juan Pond in Antarctica. *Nat. Geosci.* **3**, 341–344 (2010).

93. L. M. François, J.-C. Gérard, Reducing power of ferrous iron in the Archean ocean, 1. Contribution of photosynthetic oxygen. *Paleoceanography* **1**, 355–368 (1986).

II: Environmental states and observational discriminants. http://arxiv.org/abs/1608.08620 (2016).

94. L. A. Derry, Causes and consequences of mid-Proterozoic anoxia. *Geophys. Res. Lett.* **42**, 8538–8546 (2015).

95. S. L. Olson, L. R. Kump, J. F. Kasting, Quantifying the areal extent and dissolved oxygen concentrations of Archean oxygen oases. *Chem. Geol.* **362**, 35–43 (2013).

96. C. T. Reinhard, N. J. Planavsky, S. L. Olson, T. W. Lyons, D. H. Erwin, Earth's oxygen cycle and the evolution of animal life. *Proc. Natl. Acad. Sci. U.S.A.* **113**, 8933–8938 (2016).

97. S. M. Som, R. Buick, J. W. Hagadorn, T. S. Blake, J. M. Perreault, J. P. Harnmeijer, D. C. Catling, Earth's air pressure 2.7 billion years ago constrained to less than half of modern levels. *Nat. Geosci.* **9**, 448–451 (2016).

98. S. M. Som, D. C. Catling, J. P. Harnmeijer, P. M. Polivka, R. Buick, Air density 2.7 billion years ago limited to less than twice modern levels by fossil raindrop imprints. *Nature* **484**, 359–362 (2012).

99. B. Marty, L. Zimmermann, M. Pujol, R. Burgess, P. Philippot, Nitrogen isotopic composition and density of the Archean atmosphere. *Science* **342**, 101–104 (2013).

100. S. Ryan, E. J. Dlugokencky, P. P. Tans, M. E. Trudeau, Mauna Loa volcano is not a methane source: Implications for Mars. *Geophys. Res. Lett.* **33**, L12301 (2006).

101. C. D. K. Herd, The oxygen fugacity of olivine-phyric martian basalts and the components within the mantle and crust of Mars. *Meteorit. Planet. Sci.* **38**, 1793–1805 (2003).

102. C.-T. A. Lee, J. S. Lackey, Global continental arc flare-ups and their relation to long-term greenhouse conditions. *Elements* **11**, 125–130 (2015).

103. G. Etiope, B. Sherwood Lollar, Abiotic methane on Earth. *Rev. Geophys.* **51**, 276–299 (2013).

104. A. A. Pavlov, L. L. Brown, J. F. Kasting, UV shielding of NH_3 and O_2 by organic hazes in the Archean atmosphere. *J. Geophys. Res.* **106**, 23267–23287 (2001).

105. J. L. Linsky, K. France, T. Ayres, Computing intrinsic Lyα fluxes of F5 V to M5 V stars. *Astrophys. J.* **766**, 69–78 (2013).

Citation: J. Krissansen-Totton, S. Olson, D. C. Catling, Disequilibrium biosignatures over Earth history and implications for detecting exoplanet life. *Sci. Adv.* **4**, eaao5747 (2018).

Science Advances

Disequilibrium biosignatures over Earth history and implications for detecting exoplanet life

Joshua Krissansen-Totton, Stephanie Olson and David C. Catling

ARTICLE TOOLS	http://advances.sciencemag.org/content/4/1/eaao5747
SUPPLEMENTARY MATERIALS	http://advances.sciencemag.org/content/suppl/2018/01/22/4.1.eaao5747.DC1
REFERENCES	This article cites 86 articles, 22 of which you can access for free http://advances.sciencemag.org/content/4/1/eaao5747#BIBL
PERMISSIONS	http://www.sciencemag.org/help/reprints-and-permissions

Use of this article is subject to the Terms of Service

Supplementary Materials for

Disequilibrium biosignatures over Earth history and implications for detecting exoplanet life

Joshua Krissansen-Totton, Stephanie Olson, David C. Catling

This PDF file includes:

Supplementary Materials

Supplementary Text

section S1. The omission of solids, redox-sensitive nonvolatile aqueous species, and ocean heterogeneity

We neglected redox-sensitive, non-volatile aqueous species because they are not remotely observable, but this omission does not affect our results significantly. The most abundant redox-sensitive, non-volatile aqueous species in the Precambrian ocean was iron. If the Precambrian ocean was mostly ferruginous, then aqueous Fe^{2+} could react with O_2 or with aqueous NO_3^- derived from N_2 oxidation (92), thereby adding to the maximum Proterozoic available energy. To test this, we repeated maximum Proterozoic disequilibrium calculations using Aspen Plus and varied the concentration of ferrous iron (with zero initial ferric iron). If Fe^{2+} concentrations in the Precambrian oceans were 7×10^{-5} mol/kg (5.5×10^{-4} mol per mol of atmosphere), assuming siderite saturation (93), then only ~13 J/mol are added from Fe^{2+} oxidation, a 2% increase from the nominal maximum Proterozoic case. Even if Fe^{2+} concentrations were extremely high due to siderite supersaturation (94), for instance 3×10^{-3} mol/kg (0.023 mol per mol of atmosphere), then the available energy is 1197 J/mol. This is still less than the Phanerozoic disequilibrium, and does not change the qualitative disequilibrium evolution in Fig. 2.

By assuming saturation to obtain initial dissolved gas abundances, we are neglecting the possible contribution from ocean heterogeneity. Specifically, by adopting Henry's law to calculate the initial dissolved oxygen abundance, we may be overestimating the Proterozoic disequilibrium because the Proterozoic ocean was mostly anoxic. However, even at saturation, the number of moles of oxygen in the ocean is about two orders of magnitude less than the atmosphere, and so the total available energy will be overestimated only very slightly. If the maximum Proterozoic disequilibrium calculation is repeated with zero dissolved oxygen in the initial state, then the total available energy is only 6 J/mol lower than when oxygen saturation is assumed (<1% difference). This calculation also shows that oxygen oases in the Archean (95) and Proterozoic (96) will have a negligible effect on the global disequilibrium – a realistic Precambrian ocean with 1-10% oxic waters will yield an available energy somewhere between our O_2-saturated nominal calculation, and the zero dissolved oxygen endmembers. However, oxygen oases still represent an important example of local disequilibria maintained by life that would be very difficult to detect remotely.

section S2. Full results and Aspen Plus validation

Tables S1, S2, S3, S4, and S5 show full multiphase equilibrium results for our Proterozoic maximum, Proterozoic minimum, Proterozoic mid-level oxygen, Archean maximum, and Archean minimum scenarios, respectively.

section S3. Reactions associated with Precambrian disequilibria and their Gibbs energy contributions

Table S6 shows the various reactions contributing to Proterozoic disequilibrium, and the Gibbs energy contribution from each of these reactions. Since methane levels were potentially high in the Proterozoic, the contribution from methane oxidation (75 J/mol) to the maximum Proterozoic disequilibrium is much higher than the ~1.3 J/mol contribution to the modern Earth. Contributions from the oxidation of aqueous species such as ammonium and sulfide only contribute 14% to the total available Gibbs energy (maximum case), and are not relevant for life detection on exoplanets since changes in ocean speciation are not remotely observable.

Table S7 shows the various reactions contributing to Archean disequilibrium, and the Gibbs energy contribution from each of these reactions. The second largest contributor to maximum Archean disequilibrium (after ammonium formation from methane oxidation) is the oxidation of carbon monoxide.

section S4. Sensitivity of available Gibbs energy to difficult-to-observe variables

Table S8 shows the thermodynamic disequilibrium for our maximum Archean case where we have varied parameters such as temperature, ocean pH/alkalinity, ocean salinity, ocean volume, atmospheric pressure, and atmospheric bulk composition. Theses variables are challenging to observe for exoplanets, and so this table explores whether it would be possible to quantify the presence of thermodynamic disequilibrium for an Archean-like exoplanet. Results are reported for both Matlab and ASPEN calculations, and the two computational methods agree to within a few percent in every case, validating our Matlab calculations.

The CH_4-depleting reaction went to completion (i.e. all CH_4 was used up in a forward reaction) regardless of temperature.

Ocean alkalinity was varied by solving the carbonate system equilibria for a system with $pCO_2 = 0.5$ bar and the specified alkalinity from the table S8 (25). Next, Na(+) abundances were adjusted from their nominal values to maintain charge balance. We find that for the high alkalinity case (200 mmol/kg) the CH_4-depleting reaction only depletes 89% of the methane in equilibrium, as opposed to over 99% in other sensitivity tests. This case is highlighted in bold in table S8. However, alkalinities this high are unlikely to occur given buffering from silicate weathering (29).

Ocean salinity was varied by increasing (or decreasing) Na(+) and Cl(-) by the same amount, thereby preserving carbonate alkalinity. The CH_4-depleting reaction went to completion regardless of salinity.

Ocean volume was varied by scaling the liquid water abundances and other aqueous constituents by the specified amount. All reactions went to completion except the very low ocean volume case, which is highlighted in bold in table S8. Note that in the extreme case of no ocean, reaction (4) does not occur and the Archean disequilibrium is small (Fig. 2) and is dominated by CO oxidation (table S7). Promising strategies for constraining ocean volume remotely such as glint,

polarization, time-resolved photometry, geophysical theory, and thermal inertia, are discussed in Krissansen-Totton *et al.* (25). However, even if surface oceans cannot be directly detected, for instance because of haze obscuring surface features, then it may still be possible to infer the presence of an ocean. If water vapor abundance at a particular pressure level can be constrained, then climate models could be applied to check for consistency with a steam atmosphere.

Archean total pressure may have been less than 1 bar (97-99), and exoplanet surface pressures may vary considerably, and so we also calculate the sensitivity of our disequilibrium to total atmospheric pressure. Atmospheric pressure was varied by changing the gas-phase pressure and adjusting the liquid-to-gas ratio by the inverse amount. This accounts for Archean pressure being lower (higher) because of fewer (more) moles in the atmosphere, not because of a change in gravity. The carbonate equilibria was solved for the new initial conditions, and Na(+) abundances were adjusted to preserve charge balance. For the more extreme cases, the initial water phase separation needed to be readjusted using Henry's law (see methods). The CH_4-depleting reaction went to completion regardless of pressure, and for modest changes in pressure (0.5 bar or 2 bar), the available Gibbs energy is very similar to the 1 bar case.

Finally, we considered lower pressure in conjunction with different bulk abundances. This is relevant to the early Archean where there is considerable uncertainty in atmospheric composition. The maximum Archean disequilibrium was calculated for both 17 % N_2 with 80% CO_2, and for 77% N_2 with 20% CO_2 (the remaining 3% is water vapor and CH_4 as shown in table S4). The available energy in these cases is very similar to the nominal case (47% CO_2 and 50% N_2). Even with only 2% N_2 abundance and 95% CO_2 abundance (at 1 bar), the available energy is still comparable to the nominal case. These results imply that it is not necessary to constrain the N_2 abundance precisely in order to calculate thermodynamic disequilibrium. So long as there is enough N_2 to oxidize all the CH_4, reaction (4) will go to completion and the available energy will be large.

section S5. Abiotic CH_4 formation from high-temperature processes

Abiotic CH_4 outgassed from a highly reduced mantle would be easily distinguishable from biotic methane. The thermodynamic calculations reported here are derived in Catling and Kasting (26, Ch. 7). For temperature-pressure conditions relevant to surface volcanism (T = 1200 °C, P = 5 atm) and Earth-like oxygen fugacity for the upper mantle (near the quartz-fayalite-magnetite buffer, $f_{O_2} = 10^{-8.5}$ bar), the predicted CH_4/CO_2 ratio of magmatic gases in thermodynamic equilibrium is 9.4×10^{-11}. This result explains why negligible CH_4 is outgassed from volcanoes on the modern Earth (100), except from the thermal decomposition of organic matter.

Let us consider scenarios that might make volcanic CH_4 non-negligible. If the mantle oxygen fugacity is four orders of magnitude lower than Earth's upper-mantle, comparable to inferences from some Mars meteorites (101), then the predicted CH_4/CO_2 ratio is ~0.01. The CO_2 outgassing flux on the modern Earth is around 10 Tmol/yr (102), and so even in this extreme case the predicted methane flux is only 0.1 Tmol/yr. However, if the total outgassing flux was 1-2 orders of magnitude higher, as is possible for the early Earth, then the volcanic methane flux could extend into the Tmol/yr range, comparable to the modern biological flux. Yet in this scenario, the predicted CO/CH_4 ratio is ~6. The atmosphere of such a planet would be rich in

CO. Because CO has many readily observable spectral features (42), this planet would be easily distinguished from a CO_2-CH_4 biosignature. The coexistence of atmospheric carbon at opposite ends of the redox spectrum (+4 in CO_2 and -4 in CH_4) with no intermediate (+2) CO cannot be explained by high-temperature outgassing alone.

Other high temperature processes have been proposed for abiotic CH_4 such as iron carbonate decomposition, graphite metamorphism, clay-catalyzed hydrocarbon synthesis, and organosulfur reactions (41,103). These pathways are either unlikely to be significant on a global scale, have not been well quantified, or in the case of graphite, are likely ultimately sourced from organic carbon.

section S6. Atmospheric kinetics of methane destruction

Figure S3 shows how surface methane fluxes are related to steady state methane abundances for anoxic atmospheres. The solid black line is from Kasting and Brown (77) where a Sun-like star is assumed and a photochemical model is used to compute steady state CH_4 abundances in Earth's early atmosphere. The relationship looks similar for an Archean-Earth-like exoplanet atmosphere around M-dwarfs because the dominant sink for atmospheric methane in anoxic atmospheres is photochemical destruction and hydrogen escape (104). In steady state, the net H source to the anoxic atmosphere will be balanced by the net loss of H via escape at the top of the atmosphere

$$F_{escape} = F_{input} \text{ (of H atoms)} \tag{S1}$$

If we assume the H input source is primarily the CH_4 flux into the atmosphere, as is likely for planets with large biological CH_4 fluxes (59), and that H escape is diffusion limited, then equation (S1) becomes

$$k_{esc} f_{tot} = 4 F_{CH_4} \tag{S2}$$

where $k_{esc} = 2.5 \times 10^{13}$ cm^{-2} s^{-1} is from diffusion-limited escape theory (see below), F_{CH_4} is the CH_4 flux to the atmosphere (Tmol CH_4/yr), and we weight CH_4 fluxes by the number of H atoms per molecule.

Because of efficient turbulent mixing below the homopause, the total hydrogen mixing ratio at the homopause is the same as that immediately above the troposphere and dominated by CH_4, so

$$f_{tot} \approx 4 f_{CH_4} \tag{S3}$$

Where f_{CH_4} is the CH_4 mixing ratio. Thus by combining equations (S2) and (S3) and rearranging with a conversion factor to global Teramole (10^{12} mole) fluxes of CH_4, we have

$$f_{CH_4} = F_{CH_4} / k_{esc} = F_{CH_4} \text{ (Tmol/yr)} / 6680 \text{ (Tmol/yr)} \qquad \text{(S4)}$$

The constant $k_{esc} = b(T)/H_a(T)$, where $b(T)$ is a binary diffusion coefficient weakly dependent on the temperature at the homopause and $H_a(T)$ is the temperature-dependent scale height at the homopause (see (26) for details). Here, we assume $b(T = 208 \text{ K})/H_a(T = 208 \text{ K}) = 2.5 \times 10^{13}$ molecules cm^{-1} s^{-1} = 6680 Tmol/yr.

In fig. S3 we plot the steady state abundances derived from this diffusion-limited escape rate for homopause temperatures of T=150 K, 200 K, and 250 K, and an Earth-like scale-height (corrected for temperature). These lines provide a lower limit on CH_4 fluxes for any given CH_4 abundance. For instance, if there are other H-bearing gases (e.g. high H_2), then $f_{tot} > 4f_{CH_4}$ and the actual CH_4 flux required to maintain an observed CH_4 abundance may be higher than the diffusion limit suggests (note that a change in this direction would only strengthen the case for biology). For planets with different atmospheric bulk abundances (e.g. CO_2-dominated) or different surface gravities, the homopause scale height will change and so the diffusion limit will be slightly shifted relative to the lines plotted in fig. S3.

In principle, the diffusion limit is independent of stellar type, and so the linear relationship between fluxes and abundances in fig. S17 is expected to apply to all habitable exoplanets with anoxic atmospheres. Escape rates slower than the diffusion limit are unlikely because even for cold thermospheres, non-thermal escape process compensate for lowered Jeans' escape (68). Photodissociation of CH_4 and therefore the rate of hydrogen escape is ultimately limited by the shortwave (<145 nm) stellar flux. The dominant stellar flux at these wavelengths comes from the Lyman-α line (121.6 nm), and habitable zone planets around M stars typically receive higher Lyman-α fluxes than habitable zones planets around G stars (105). We therefore expect hydrogen escape around M stars to be limited by diffusion, and not by CH_4 photodissociation.

Figure S3 suggests that CH_4 abundances in excess of 1.5×10^{-3} imply surface fluxes in excess of 10 Tmol CH_4/yr, which is likely biological (Fig. 6), whereas CH_4 abundances in excess of 10^{-2} imply surface fluxes in excess of 50 Tmol CH_4/yr, which is very likely biological (Fig. 6). Today's flux of CH_4 to the Earth's atmosphere is ~30 Tmol CH_4/yr, for comparison.

Naturally, the calculations outlined above are to be interpreted as approximations. If methane is observed on a nearby exoplanet, then photochemical modeling using the observed stellar spectrum might be attempted to produce a more precise version of fig. S3. Once CH_4 abundances have been constrained by observation, the corresponding escape flux, and by extension the surface source flux can be inferred. This can then be compared to the likely distribution of maximum abiotic source fluxes.
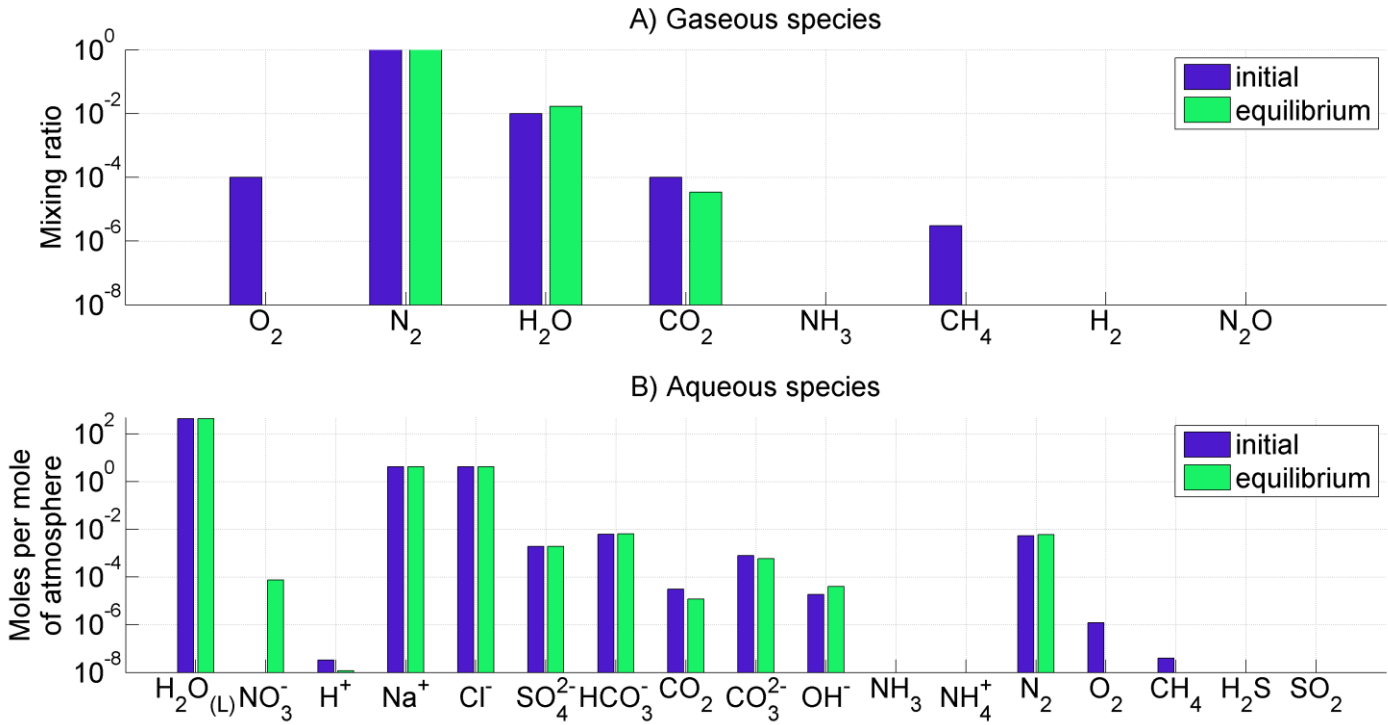
fig. S1. Atmosphere-ocean disequilibrium in the Proterozoic (minimum disequilibrium scenario). Blue bars denote assumed initial abundances from the literature, and green bars denote equilibrium abundances calculated using Gibbs free energy minimization. Subplots separate (**A**) atmospheric species and (**B**) ocean species.
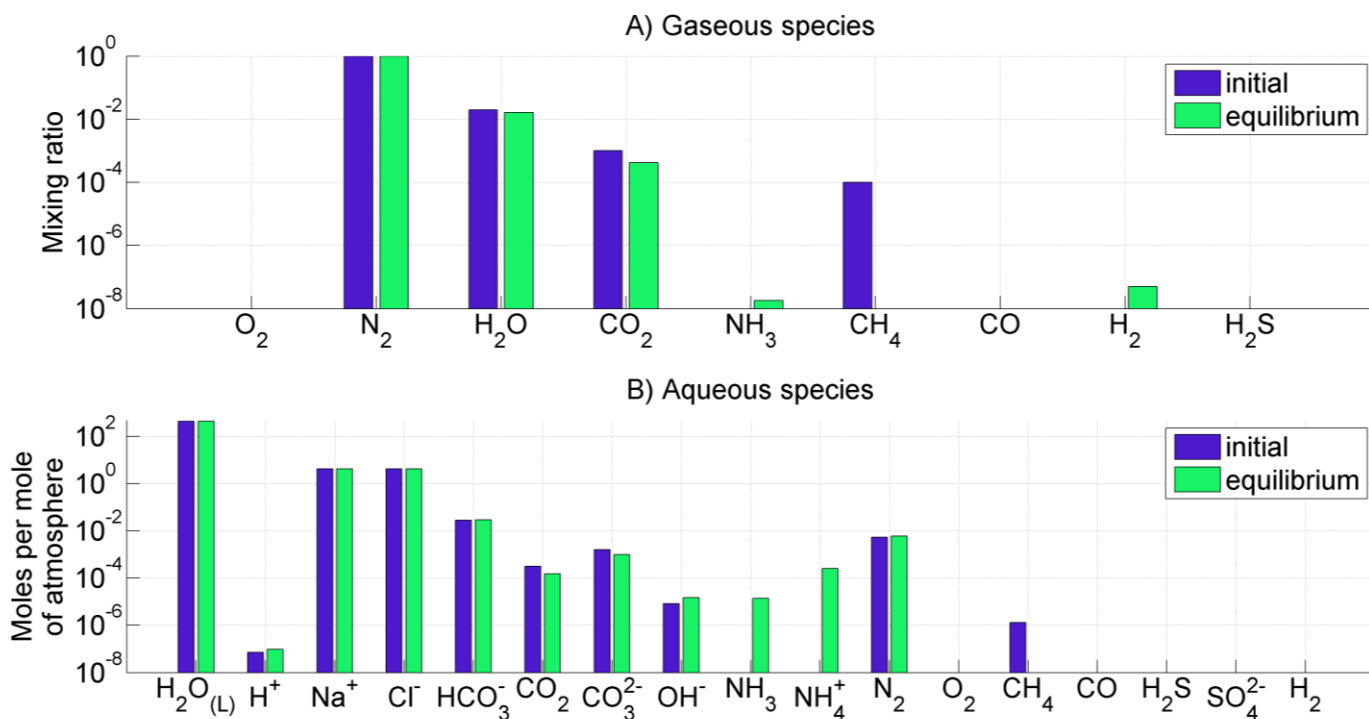
fig. S2. Atmosphere-ocean disequilibrium in the Archean (minimum disequilibrium scenario). Blue bars denote assumed initial abundances from the literature, and green bars denote equilibrium abundances calculated using Gibbs free energy minimization. Subplots separate (**A**) atmospheric species and (**B**) ocean species. Note that even in the minimum disequilibrium case, atmospheric CH_4 is depleted by reaction to equilibrium.
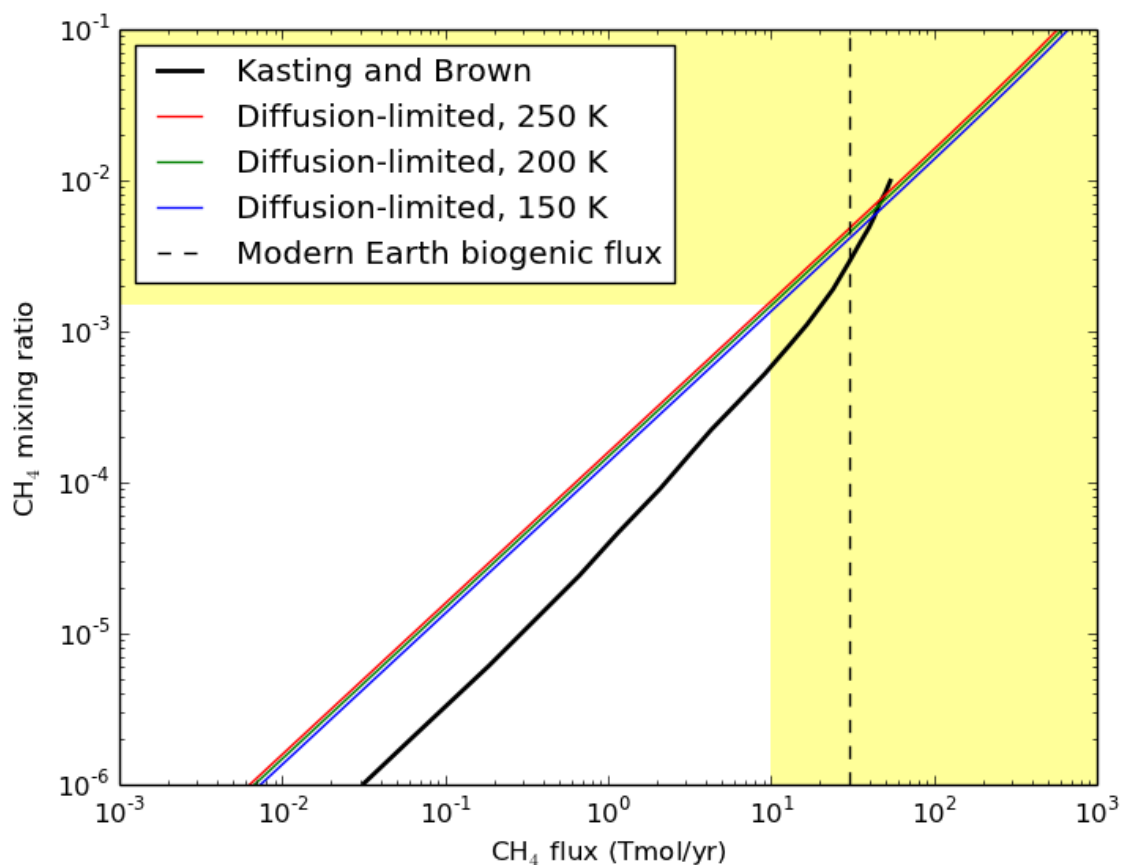
fig. S3. Relationship between methane fluxes and atmospheric abundances. The black line is derived in (77) using a photochemical model for the early Earth's atmosphere, assuming a Sun-like star. The red, green, and blue lines are derived assuming diffusion-limited escape of hydrogen with homopause temperatures of 250 K, 200 K, and 150 K, respectively. Diffusion-limited escape demarcates the minimum methane flux required to sustain any given methane abundance. Note that the diffusion-limited escape model may overestimate the CH_4 mixing ratio at any given flux by a factor of 2-3 because it does not account for other CH_4 sinks.

table S1. Proterozoic maximum disequilibrium. Mixing ratios are reported for gaseous species, and moles per mole of atmosphere for aqueous species. Note that final Aspen values that do not completely conserve mass and charge are an artifact of Aspen automatically adjusting initial abundances slightly before performing Gibbs energy calculations.

	Initial	Matlab final	Aspen final
H_2O(liquid)	436.788155	436.793984	436.7938
O_2	0.03	2.64E-05	5.59E-05
N_2	0.86	0.84759313	0.8485178
H_2O	0.01	0.01627808	0.0163399
CO_2	0.1	0.11308654	0.1148073
NH_3	1.00E-15	3.47E-12	0
CH_4	0.0001	1.29E-12	0
H_2	2.00E-06	5.32E-12	0
N_2O	1.00E-06	1.47E-11	0
$NO_3(-)$	7.83E-15	0.02387899	0.0238104
$H(+)$	8.74E-06	0.001014	0.00119341
$Na(+)$	4.3773073	4.3773073	4.338146
$Cl(-)$	4.27587006	4.27587006	4.237616
$SO_4(2-)$	0.03916493	0.03916493	0.0388458
$HCO_3(-)$	0.02348567	0.00024239	0.000221296
CO_2(aq)	0.03135339	0.04162247	0.0397126
$CO_3(2-)$	1.10E-05	9.20E-10	3.38E-10
$OH(-)$	7.02E-08	1.00E-15	4.13E-10
NH_3(aq)	7.79E-13	3.89E-12	0
$NH_4(+)$	0.00039165	4.61E-12	0
N_2(aq)	0.00470212	0.00536632	0.0044815
O_2(aq)	0.00037233	3.37E-07	5.91E-07
CH_4(aq)	1.32E-06	1.28E-12	0
H_2S(aq)	1.00E-15	1.52E-12	0
SO_2(aq)	7.83E-15	4.58E-12	0
Available Gibbs energy, Φ (J/mol)		**884**	**860**

table S2. Proterozoic minimum disequilibrium. Mixing ratios are reported for gaseous species, and moles per mole of atmosphere for aqueous species. Note that final Aspen values that do not completely conserve mass and charge are an artifact of Aspen automatically adjusting initial abundances slightly before performing Gibbs energy calculations.

	Initial	Matlab final	Aspen final
H_2O(liquid)	436.7881549	436.7814412	436.7812
O_2	0.0001	2.64E-12	0
N_2	0.99	0.989253694	0.9894527
H_2O	0.01	0.01657188	0.0167461
CO_2	0.0001	3.39E-05	1.25128E-05
NH_3	1.00E-15	4.09E-12	0
CH_4	3.00E-06	1.44E-12	0
H_2	1.00E-15	1.45E-11	0
N_2O	1.00E-15	1.33E-11	0
$NO_3(-)$	7.83E-15	7.61E-05	7.61295E-05
$H(+)$	3.28E-08	1.20E-08	1.56172E-08
$Na(+)$	4.287638267	4.287638267	4.28568
$Cl(-)$	4.275870063	4.275870063	4.273917
$SO_4(2-)$	0.001958246	0.001958246	0.00195735
$HCO_3(-)$	0.006265174	0.00653947	0.00658799
CO_2(aq)	3.14E-05	1.21E-05	4.57563E-06
$CO_3(2-)$	7.84E-04	5.98E-04	5.75E-04
$OH(-)$	1.87E-05	4.02E-05	3.36E-05
NH_3(aq)	7.79E-13	4.40E-12	0
$NH_4(+)$	7.83E-15	4.62E-12	0
N_2(aq)	0.005412906	0.006121147	0.00592217
O_2(aq)	1.24E-06	7.42E-11	0
CH_4(aq)	3.96E-08	1.42E-12	0
H_2S(aq)	7.83E-15	1.46E-12	0
SO_2(aq)	7.83E-15	4.08E-12	0
Available Gibbs energy, Φ (J/mol)		**9.54**	**9.26**

table S3. Proterozoic disequilibrium with 2% PAL of O_2. Mixing ratios are reported for gaseous species, and moles per mole of atmosphere for aqueous species. The available energy from this scenario separates the lightly and darkly shaded region in Fig. 2. Note that final Aspen values that do not completely conserve mass and charge are an artifact of Aspen automatically adjusting initial abundances slightly before performing Gibbs energy calculations.

	Initial	final matlab	final - ASPEN
H_2O(liquid)	436.7882	436.7825	436.7822
O_2	0.004	1.00E-15	3.55854E-08
N_2	0.985897	0.983636	0.9887316
H_2O	0.01	0.016433	0.0167926
CO_2	0.0001	0.001867	0.0019125
NH_3	1.00E-15	7.77E-13	0
CH_4	3.00E-06	5.83E-14	0
H_2	1.00E-15	1.27E-12	0
N_2O	1.00E-15	3.27E-12	0
$NO_3(-)$	7.83E-15	0.003196	0.0031961
$H(+)$	3.28E-08	8.36E-07	9.05431E-07
$Na(+)$	4.287638	4.287638	4.28568
$Cl(-)$	4.27587	4.27587	4.273917
$SO_4(2-)$	0.001958	0.001958	0.00195735
$HCO_3(-)$	0.006265	0.004645	0.00463422
CO_2(aq)	3.14E-05	0.000666	0.000624464
$CO_3(2-)$	7.84E-04	5.57E-06	9.08882E-06
$OH(-)$	1.87E-05	5.25E-07	5.30271E-07
NH_3(aq)	7.79E-13	8.48E-13	0
$NH_4(+)$	7.83E-15	9.07E-13	0
N_2(aq)	0.005413	0.006076	0.00508327
O_2(aq)	1.24E-06	7.14E-10	3.6597E-10
CH_4(aq)	3.96E-08	2.77E-13	0
H_2S(aq)	7.83E-15	2.79E-13	0
SO_2(aq)	7.83E-15	8.60E-13	0
Available Gibbs energy, Φ (J/mol)		**135**	**128**

table S4. Archean maximum disequilibrium. Mixing ratios are reported for gaseous species, and moles per mole of atmosphere for aqueous species. Note that final Aspen values that do not completely conserve mass and charge are an artifact of Aspen automatically adjusting initial abundances slightly before performing Gibbs energy calculations.

	Initial	final matlab	final - ASPEN
H_2O(liquid)	436.77573	436.734522	436.9592
O_2	2.00E-07	1.63E-13	0
N_2	0.5	0.48682701	0.4874388
H_2O	2.00E-02	0.01591615	0.0158566
CO_2	0.47	0.44878826	0.4465212
NH_3	1.00E-09	1.59E-08	1.97E-08
CH_4	0.01	1.91E-05	3.48E-05
CO	0.001	1.00E-15	1.08E-11
H_2	0.0001	5.98E-08	7.05E-08
H_2S	3.1326E-05	0.0004157	0.00047851
H(+)	3.29E-06	3.02E-06	3.16E-06
Na(+)	4.59192496	4.59192496	4.594223
Cl(-)	4.28E+00	4.27587006	4.277862
HCO_3(-)	0.31253612	0.3402181	0.3402828
CO_2(aq)	0.16551098	0.17043556	0.172843
CO_3(2-)	0.00039017	0.00011673	0.00020317
OH(-)	1.87E-07	1.49E-07	1.60E-07
NH_3(aq)	7.79E-07	1.36E-05	1.26E-05
NH_4(+)	0.00039165	0.02585194	0.0256976
N_2(aq)	0.00273379	0.00317021	0.00263621
O_2(aq)	2.03E-09	1.31E-14	0
CH_4(aq)	0.00013211	3.01E-07	4.21E-07
CO(aq)	8.66E-06	1.24E-12	8.62E-14
H_2S(aq)	3.13E-05	0.00048445	0.00046404
SO_4(2-)	0.0015666	0.00072908	0.00068588
H_2(aq)	6.48E-07	3.28E-11	4.19E-10
Available Gibbs energy, Φ (J/mol)		**234**	**232**

table S5. Archean minimum disequilibrium. Mixing ratios are reported for gaseous species, and moles per mole of atmosphere for aqueous species. Note that final Aspen values that do not completely conserve mass and charge are an artifact of Aspen automatically adjusting initial abundances slightly before performing Gibbs energy calculations.

	initial	final matlab	final - ASPEN
H_2O(liquid)	436.77573	436.778199	437.0025
O_2	1.00E-15	5.17E-13	0
N_2	0.98	0.979146	0.9801331
H_2O	2.00E-02	0.01647763	0.0166226
CO_2	0.001	0.00042043	0.00057407
NH_3	1.00E-15	1.80E-08	1.51E-08
CH_4	0.0001	9.40E-09	7.91E-09
CO	1.00E-15	8.58E-12	0
H_2	1.00E-15	5.03E-08	4.85E-08
H_2S	7.83E-15	7.83E-15	0
H(+)	7.29E-08	9.70E-08	4.38E-08
Na(+)	4.30721038	4.30721038	4.30721
Cl(-)	4.28E+00	4.27587006	4.27587
HCO_3(-)	0.02816377	0.02960221	0.0292059
CO_2(aq)	0.00031353	0.00015015	0.00019063
CO_3(2-)	0.00158412	9.90E-04	0.00119208
OH(-)	8.38E-06	1.47E-05	1.10E-05
NH_3(aq)	7.83E-15	1.37E-05	9.33E-06
NH_4(+)	7.83E-15	0.00025639	0.00026079
N_2(aq)	0.00535822	6.08E-03	0.00509003
O_2(aq)	1.00E-15	5.01E-13	0
CH_4(aq)	1.32E-06	9.88E-11	9.18E-11
CO(aq)	1.00E-15	5.73E-12	0
H_2S(aq)	7.83E-15	7.83E-15	0
SO_4(2-)	7.83E-15	7.83E-15	0
H_2(aq)	1.00E-15	2.21E-10	2.77E-10
Available Gibbs energy, Φ (J/mol)		**5.1**	**3.4**

table S6. Reactions contributing to Proterozoic disequilibrium. Note that the contributing Gibbs energies do not sum exactly to the total available energy because there are additional contributions from water activity changes, and because reactions are not independent.

Description	Reaction	Contribution to maximum disequilibrium	Contribution to minimum disequilibrium
Nitrate formation	$5O_2 + 2N_2 + 2H_2O \rightarrow 4H^+ + 4NO_3^-$	640 J/mol (72%)	7.4 J/mol (79%)
Carbonate speciation from ocean acidification	$HCO_3^- + H^+ \rightarrow H_2O + CO_2$		
Ammonium oxidation	$3O_2 + 4NH_4^+ \rightarrow 6H_2O + 4H^+ + 2N_2$	101 J/mol (11%)	0 J/mol (0%)
Methane oxidation	$CH_4 + 2O_2 \rightarrow 2H_2O + CO_2$	75 J/mol (8%)	2.1 J/mol (23%)
Sulfide oxidation	$H_2S + 2O_2 \rightarrow 2H^+ + SO_4^{2-}$	27 J/mol (3%)	0 J/mol (0%)
Total available Gibbs energy		884 J/mol	9.5 J/mol

table S7. Reactions contributing to Archean disequilibrium. Note that the contributing Gibbs energies do not sum exactly to the total available energy because there are additional contributions from water activity changes, and because reactions are not independent. For instance, hydrogen oxidation produces methane that then adds to ammonium formation.

Description	Reaction	Contribution to maximum disequilibrium	Contribution to minimum disequilibrium
Ammonium formation	$5CO_2 + 4N_2 + 3CH_4 + 14H_2O \rightarrow 8NH_4^+ + 8HCO_3^-$	170 J/mol (74%)	4 J/mol (80%)
Carbon monoxide oxidation	$4CO + 2H_2O \rightarrow 3CO_2 + CH_4$	42 J/mol (18%)	0 J/mol (0%)
Hydrogen oxidation	$CO_2 + 4H_2 \rightarrow 2H_2O + CH_4$	2 J/mol (1%)	0 J/mol (0%)
Sulfate reduction	$CO_2 + CH_4 + SO_4^{2-} \rightarrow H_2S + 2HCO_3^-$	3 J/mol (1%)	0 J/mol (0%)
Carbon speciation	$H_2O + CO_2 + CO_3^{2-} \rightarrow 2HCO_3^-$	<1 J/mol (<1%)	1 J/mol (20%)
Ammonia formation	$N_2 + 3H_2 \rightarrow 2NH_3$	<1 J/mol (<1%)	0 J/mol (0%)
Total available Gibbs energy		231 J/mol	5.1 J/mol

table S8. Sensitivity of Archean disequilibrium to difficult-to-observe variables.
Disequilibria values highlight in bold indicate scenarios where methane-depletion did not occur (<90% depletion). Available energies are reported for both our Matlab calculations, and the commercial software package Aspen Plus, and the two methods are in agreement.

		Available Gibbs free energy (J/mol)	
		Matlab	ASPEN
Temperature, K	273.15	369	359
	288.15	234	232
	298.15	220	204
Ocean alkalinity, mmol/kg (pH)	4 (pH=5.4)	363	359
	40 (pH=6.4)	234	232
	200 (pH=7.1)	152	**181**
Ocean salinity, relative to modern	0.1	199	198
	1	234	232
	10	249	223
Ocean volume, relative to modern	0.1	**89**	**89**
	0.5	188	187
	1	234	232
	2	279	277
	10	405	401
	50	701	682
Atmospheric pressure, atm	0.1	125	141
	0.5	220	213
	1	234	232
	2	271	262
	10	366	354
Low pressure (0.5 bar) and variable bulk abundances	17% N_2, 80% CO_2	198	191
	50% N_2, 47% CO_2	220	213
	77% N_2, 20% CO_2	224	214
Low N2 abundance	2% N_2, 95% CO_2	151	150
	50% N_2, 47% CO_2	234	232